Physics of Fluids

Scale-resolving turbulent channel flow simulations using a dynamic cumulant lattice Boltzmann method

Cite as: Phys. Fluids **34**, 075129 (2022); https://doi.org/10.1063/5.0098032
Submitted: 04 May 2022 • Accepted: 28 June 2022 • Accepted Manuscript Online: 28 June 2022 • Published Online: 22 July 2022

Martin Gehrke and Thomas Rung

Physics of Fluids ARTICLE scitation.org/journal/phf

Scale-resolving turbulent channel flow simulations using a dynamic cumulant lattice Boltzmann method

Cite as: Phys. Fluids **34**, 075129 (2022); doi: 10.1063/5.0098032
Submitted: 4 May 2022 · Accepted: 28 June 2022 ·
Published Online: 22 July 2022

View Online Export Citation CrossMark

Martin Gehrke[a] and Thomas Rung

AFFILIATIONS

Hamburg University of Technology, Institute for Fluid Dynamics and Ship Theory, Am Schwarzenberg-Campus 4, 21073 Hamburg, Germany

[a]Author to whom correspondence should be addressed: martin.gehrke@tuhh.de

ABSTRACT

This paper reports the assessment of a modified cumulant lattice Boltzmann method in turbulent channel flows. The suggested approach is of interest for its resolution-spanning capabilities, which are scrutinized for grid resolutions between 4 and 430 wall units. With the emphasis on a recently published parameterized cumulant collision operator, we suggest a resolution-sensitive regularization supplemented by a dynamic subgrid-scale model based upon third-order cumulant expressions, which seamlessly vanishes for direct numerical simulations. The strategy is optionally supplemented by a wall function approach to adjust the wall treatment. The analysis involves the mean flow field, resolved and modeled second moments, two-point correlations, and spectral data and correlation lengths obtained for four friction Reynolds numbers (180, 550, 2000, and 5200). Results display a resolution-independent capability to simulate the attached turbulent shear flow.

I. INTRODUCTION

The lattice Boltzmann method (LBM) is gaining increased attention for the efficient simulation of industrial flows.[1–5] Since engineering flows are mostly turbulent, the predictive success of LBM in turbulent flows has recently been addressed in several studies.[6–13] As indicated in the literature, the accuracy in turbulent flow predictions strongly depends on the employed collision operator,[14–16] and modifications to the collision operator are, therefore, a central area of LBM research. Various suggestions to increase the stability and accuracy of LBM in turbulent flows were published. Related research is often devoted to the relaxation of distribution functions, where either the relaxation rates[17,18] or the relaxation space[6,19–22] is the subject of the investigations. A comprehensive review of the many collision operator models and their rationale is beyond the scope of this paper, and we refer to a recent review of Coreixas *et al.*[23]

This paper is devoted to a modified cumulant collision operator[22] for turbulent flow simulations. The cumulant collision model suggests relaxing the distribution functions in cumulant space. Scale-resolving simulations of turbulent shear flows using the cumulant model were previously studied by, e.g., Geier *et al.*,[12,22] Pasquali *et al.*,[24] or Gehrke *et al.*[14,25,26] While indicating a promising predictive performance, virtually, all these studies were restricted to reasonably generic flows and a narrow range of resolutions in the regime of direct numerical simulations (DNS) and wall-resolved large eddy simulations (LES). An exception refers to a recent study of the present authors on the predictive performance of the well-conditioned parameterized (WP) cumulant model[27] in separated flows over periodic hills,[26] which involved a comprehensive range of (bulk) Reynolds numbers and resolutions ranging from $700 \leq \mathrm{Re} \leq 37.000$ and $1 \leq \Delta x^+ \leq 60$. Results reveal that a stability preserving regularization inherent to the WP cumulant model acts as a subgrid-scale (SGS) model confined to the upper dissipative frequencies by addressing higher, i.e., third-order, relaxation rates. Moreover, the variation of a single regularization parameter, which is usually assigned to a constant value, was identified as a potential starting point for resolution-dependent modifications that could improve the predictive accuracy. At the same time, the stability of the simulation suffered for coarser resolutions at higher Reynolds numbers disregarding the changes in the regularization parameter. This suggests the additional use of a subgrid-scale (SGS) model for such configurations. Both aspects, a resolution-sensitive regularization and a cumulant-based SGS model, are the focus of the present paper.

The remainder of this paper is structured as follows. Section II provides details of the numerical method, describes the employed cumulant LBM, and outlines the suggested modifications. Section III presents test case specific computational aspects. Attention is confined to a turbulent shear flow in unidirectional channels for the range of Reynolds numbers $\mathrm{Re}_\tau = u_\tau H/\nu$ based on the half channel height H and the friction velocity u_τ. Calculations employ isotropic, homogeneous grids with a lattice spacing Δx featuring a range of resolutions including $4 \leq \Delta x^+ (= \Delta x\, u_\tau/\nu) \leq 430$. Details of the employed data recording and data processing are summarized in Sec. IV. Section V is devoted to the comprehensive presentation of results. Final conclusions are drawn in Sec. VI. Supplementary information on the employed wall function and the implementation of the cumulant collision operator is given in the Appendixes.

II. NUMERICAL METHOD

Section II briefly outlines the key aspects of the employed LBM, in particular the relaxation part. Moreover, details of the SGS model and the applied wall function are given.

A. Lattice Boltzmann procedure

The current study is based on a GPU-based (graphics processing unit) lattice Boltzmann[28–32] implementation[33] for the simulation of incompressible fluid flow.[34,35] The discretized approximation is partitioned into two steps and reads

$$f^*_{ijk}(\boldsymbol{x}, t) = f_{ijk}(\boldsymbol{x}, t) + \Omega_{ijk} \quad \text{(collision step)}, \tag{1}$$

$$f_{ijk}(\boldsymbol{x} + \boldsymbol{e}_{ijk}\Delta t, t + \Delta t) = f^*_{ijk}(\boldsymbol{x}, t) \quad \text{(propagation step)}. \tag{2}$$

Herein, f_{ijk} represents particle distribution functions (PDFs), which describe the probability of a particle to be located at $\boldsymbol{x}$ in the three-dimensional space at time t moving in the direction of $\boldsymbol{e}_{ijk}$. The latter matches a directional speed matrix $\boldsymbol{e}_{ijk} = c \times (i, j, k)$ restricting the particle advection (2) to their immediate next neighbor nodes. Macroscopic flow properties are recovered by $\rho = \sum_{ijk} f_{ijk}$ and $\mathbf{u} = (u, v, w)^\top = (\sum_{ijk} \boldsymbol{e}_{ijk} f_{ijk})/\rho$.

All simulations rest upon a regular D3Q27 lattice, as outlined by Fig. 1, and assume a unit spatial (Δx) and temporal (Δt) spacing together with a lattice speed $c = \Delta x/\Delta t = 1$. The directions $i, j, k \in (\bar{1}, 0, 1)$ follow from the Miller notation ($-1 \equiv \bar{1}$, $0 \equiv 0$, $1 \equiv 1$).

The first step (1) depicts the collision step, where the incoming particle distribution function $f_{ijk}(\boldsymbol{x}, t)$ deviates from equilibrium state, and the asterisk represents the post-collisional PDF state. The symbol Ω_{ijk} denotes the collision operator, which models the interaction of the particles. In the present study, the collision proceeds in cumulant space,[22,27] whereby $\Omega_{ijk} = \Omega_{ijk}(C_{\alpha\beta\gamma})$ applies, viz.,

$$C^*_{\alpha\beta\gamma} = C^{\mathrm{eq}}_{\alpha\beta\gamma} + (1 - \omega_{\alpha\beta\gamma})\, C_{\alpha\beta\gamma} \tag{3}$$

with the cumulant expressions $C_{\alpha\beta\gamma}$. The Greek indices correlate with the cumulants' order and reach from zero (C_{000}) to six (C_{222}), i.e., $\alpha, \beta, \gamma \in (0, 1, 2)$. The transformation relations between the PDF and the cumulant space involve central moments through PDF space (f_{ijk}) $\rightleftarrows$ central moments $\rightleftarrows$ cumulants ($C_{\alpha\beta\gamma}$) and are omitted to safe space. Related details and an outline of the cumulant theory can be found in the seminal work of Geier *et al.*[27] Expression (3) comprises the relaxation toward specifically defined equilibria, indicated by the superscript eq, using order-dependent relaxation rates $\omega_{\alpha\beta\gamma}$ of the pre-collisional cumulant states. The choice of the relaxation rates and their regularization in high Reynolds number flows are important aspects of the present paper and are outlined below.

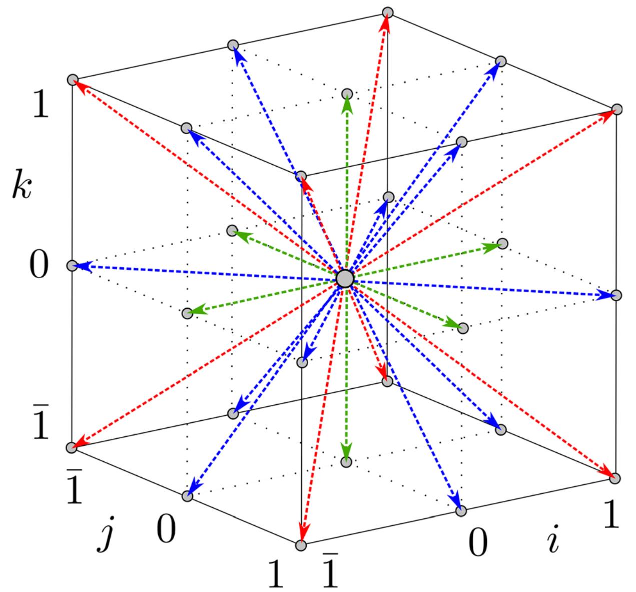

FIG. 1. D3Q27 lattice model of the present LBM. Arrows indicate the 27 discrete velocity vectors $\boldsymbol{e}_{ijk}$. Collocation points of the stencil are marked in gray.

B. Relaxation rates

Generally, the rates $\omega_{\alpha\beta\gamma}$ can be chosen within the interval $[0, 2]$, where unit values of $\omega_{\alpha\beta\gamma}$ indicate a relaxation to the equilibrium state, cf. (3). Confining our interest to the ten linear independent cumulant expressions $C_{\alpha\beta\gamma}$ and the related ten out of 27 $\omega_{\alpha\beta\gamma}$, the triple index is conveniently replaced by a single index $\omega_{\alpha\beta\gamma} = \omega_\chi$, viz., $\chi \in \{1; \ldots; 10\}$. Only two out of ten rates, i.e., ω_1 and ω_2, are linked to physical fluid properties. The relaxation rate ω_1 is determined by the (shear) viscosity ν,

$$\omega_{1,\mathrm{SI}} = \left(\frac{1}{\nu/c_s^2 + \Delta t/2}\right)_{\mathrm{SI}}, \tag{4}$$

with $c_s = c/\sqrt{3}$ as the speed of sound in the lattice and the subscript SI to denote the dimensional form in physical quantities. The relaxation rates are only employed in non-dimensional LB units during the simulation. LB units ground on the aforementioned unit spacing $\Delta x = 1, \Delta t = 1$ ($\rightarrow c = 1$), and a non-dimensional viscosity ν, which returns

$$\omega_1 = \frac{2}{6\nu + 1}. \tag{5}$$

The rate ω_2 is theoretically related to the bulk viscosity. However, the influence of a parameterized ω_2-value is beyond the scope of the present study, and we assign ω_2 to a stability promoting unit value, in line with the vast majority of previous studies. Likewise, we follow the suggestion of Geier *et al.*[27] and assign $\omega_6 = \omega_7 = \omega_8 = \omega_9 = \omega_{10} = 1$, since they address the higher (fourth- to sixth)-order cumulants' collision, and unit values yield beneficial stability properties. The three remaining rates ω_3, ω_4, and ω_5 govern third-order collision. Based on the work of Geier *et al.*,[27] these three rates can be parameterized as functions of ω_1 and ω_2. In conjunction with $\omega_2 = 1$, the parameterization reads

$$\omega_3 = \frac{8\left(2\omega_1^2 - 3\omega_1 - 2\right)}{7\omega_1^2 - 14\omega_1 - 8}, \tag{6}$$

$$\omega_4 = \frac{8\left(4\omega_1^2 - 15\omega_1 + 14\right)}{9\omega_1^2 - 50\omega_1 + 56}, \tag{7}$$

$$\omega_5 = \frac{24\left(3\omega_1^3 - 13\omega_1^2 + 12\omega_1 + 4\right)}{29\omega_1^3 - 130\omega_1^2 + 152\omega_1 + 48}. \tag{8}$$

Vanishing ω_1 yields $\omega_{\{3;4;5\}} = 2$; likewise, all $\omega_{\{3;4;5\}}$ vanish at $\omega_1 = 2$. Mind that so far, the collision modeling fully agrees with the work of Geier *et al.*[27]

1. Regularization of relaxation rates

As indicated by (5), the ω_1-value approaches two in the low-viscosity or high-Reynolds number limit and, thereby, yields vanishing third-order rates $\omega_{\{3;4;5\}} \to 0$. Negligibly small relaxation rate values virtually imply retaining the pre-collision cumulant states during the collision. This is equivalent to preserving the nonequilibrium parts, which, in turn, hampers the numerical stability. To regularize the third-order relaxation rates in the limit $\omega_{\{3;4;5\}} \to 0$, Geier *et al.*[27] suggested a regularization of the parameterization via (6)–(8), which is frequently labeled the well-conditioned parameterized (WP) cumulant model, viz.,

$$\omega^{\mathrm{R}}_{\{3;4;5\}_\varepsilon} = \omega_{\{3;4;5\}} + \frac{\mathbf{C}_\varepsilon(1-\omega_{\{3;4;5\}})}{\mathbf{C}_\varepsilon + (\rho\lambda)} = \frac{\mathbf{C}_\varepsilon + (\rho\lambda)\omega_{\{3;4;5\}}}{\mathbf{C}_\varepsilon + (\rho\lambda)}. \tag{9}$$

Here, $\mathbf{C}_\varepsilon$ refers to a positive third-order cumulant related expression, e.g., $|C_{120} - C_{102}|$, and ρ is a normalized density close to unity. The suffix ε points toward different transformation parts that employ the regularized rates using different cumulant expressions $\mathbf{C}_\varepsilon$, cf. below. The regularization (9) is controlled by a positive parameter λ. The respective limit states yield $\lim_{\lambda\to\infty} \omega^{\mathrm{R}}_{\{3;4;5\}_\varepsilon} = \omega_{\{3;4;5\}}$ and $\lim_{\lambda\to 0} \omega^{\mathrm{R}}_{\{3;4;5\}_\varepsilon} = 1$. The regularization parameter is usually assigned to an empirically identified constant value ($\lambda = 10^{-2}$), which follows from typical values of $\mathbf{C}_\varepsilon$ and $\omega_{\{3;4;5\}}$. The regularization (9) greatly supports the robustness of the WP model. For example, Geier *et al.*[12] computed a sphere at a very high Reynolds number without a turbulence model, and the present authors reported periodic hill flow (PHF) simulations without a turbulence model[26] for coarse discretizations up to $\Delta x^+ \approx 100$. However, the latter study also revealed that the predictive accuracy could significantly improve from an increase in λ when the resolution is in a typical LES-regime within $10 \le \Delta x^+ \le 50$.

Analyzing the regularization (9) for attached and separated engineering shear flows at different resolutions reveals generally small values of $\mathbf{C}_\varepsilon \approx 10^{-3} \ll \rho\lambda$ and motivates to estimate $\omega^{\mathrm{R}}_{\{3;4;5\}_\varepsilon} \approx \omega_{\{3;4;5\}} + \mathbf{C}_\varepsilon/(\rho\lambda)$. Moreover, typical relaxation rate values read $\omega_{\{3;4;5\}} \approx \mathcal{O}(10^{-3}) - \mathcal{O}(10^{-2})$. This indicates that subtle additions of $\omega_{\{3;4;5\}}$ on the order of $\mathbf{C}_\varepsilon/(\rho\lambda) \approx 0.1$ can have a distinct influence and motivates suggesting an increase[26] of λ to reduce $\mathbf{C}_\varepsilon/(\rho\lambda)$ and attenuate the shift of $\omega^{\mathrm{R}}_{\{3;4;5\}_\varepsilon}$ toward equilibrium restoring unit values. A more rigorous analysis starts by recalling that the viscosity-related relaxation rate approaches a value of $\omega_1 = 2$ in the high-Reynolds number limit of (5). With a focus on turbulent flows, we, therefore, assume $\omega_1 \approx 2 - \varepsilon$, where ε is a small positive number and introduce this approximation into the parameterization (6)–(8). Linearizing the resulting expressions for small values of ε, one obtains

$$\lim_{\varepsilon\to 0} \omega_3 = \frac{40\varepsilon}{14\varepsilon + 8} \approx 5(2-\omega_1), \tag{10}$$

$$\lim_{\varepsilon\to 0} \omega_4 = \frac{-8\varepsilon}{14\varepsilon - 8} \approx (2-\omega_1), \tag{11}$$

$$\lim_{\varepsilon\to 0} \omega_5 = \frac{96\varepsilon}{20\varepsilon + 64} \approx 1.5\,(2-\omega_1). \tag{12}$$

A resolution-aware description of the high-Reynolds number limit of ω_1 could employ the approximations (10)–(12) to derive a resolution-sensitive regularization of $\omega_{\{3;4;5\}}$. The latter is obtained from a simple analysis of the dimensional expression (4), which introduces the cell Reynolds number $\mathrm{Re}_{\Delta x} = (u\,\Delta x/\nu)_{\mathrm{SI}}$ as a measure for the resolution. Here, u_{SI} is a problem characterizing velocity, for example, the centerline velocity of a channel, or the bulk velocity of the problem, viz.,

$$\omega_{1,\mathrm{SI}} = \left(\frac{1}{\frac{3\nu}{c^2} + \frac{\Delta t}{2}}\right)_{\mathrm{SI}} = \left(\frac{2}{\frac{6u\,\Delta x}{c^2\,\mathrm{Re}_{\Delta x}} + \Delta t}\right)_{\mathrm{SI}}. \tag{13}$$

The LBM is a weakly compressible approach associated with a user-defined Mach number. The Mach number $\mathrm{Ma} = (u/c_s)_{\mathrm{SI}}$ essentially defines the time step size $\Delta t_{\mathrm{SI}} = \Delta x_{\mathrm{SI}}\,\mathrm{Ma}/\left(\sqrt{3}u_{\mathrm{SI}}\right)$ of the method in dimensional units and is used to replace the velocity in (13), viz., $u_{\mathrm{SI}} = \mathrm{Ma}\,c_{\mathrm{SI}}/\sqrt{3}$. Owing to the unit spacing concept with $\Delta x = 1$ and $\Delta t = 1$ and the definition of the lattice speed $c = \Delta x/\Delta t$, we obtain an equivalent non-dimensional expression of (13) via

$$\begin{aligned} \omega_{1,\mathrm{SI}} &= \left(\frac{2}{\frac{2\sqrt{3}\mathrm{Ma}\,\Delta x}{c\,\mathrm{Re}_{\Delta x}} + \Delta t}\right)_{\mathrm{SI}}, \\ \rightarrow \quad \omega_1 &= \frac{2\mathrm{Re}_{\Delta x}}{2\sqrt{3}\mathrm{Ma} + \mathrm{Re}_{\Delta x}} \\ &= 2 - \frac{4\sqrt{3}\mathrm{Ma}}{2\sqrt{3}\mathrm{Ma} + \mathrm{Re}_{\Delta x}} \approx 2 - \beta\frac{\mathrm{Ma}}{\mathrm{Re}_{\Delta x}}. \end{aligned} \tag{14}$$

Mind that β is of the order $\mathcal{O}(10^0)$ but can vary slightly, depending on the velocities that are employed to define the Mach and the Reynolds numbers, as the Mach number is usually compiled from an augmented velocity value. Combining (10)–(12) with (14), we conclude

$$2 - \omega_1 \sim \lim_{\varepsilon\to 0} \omega_{\{3;4;5\}} \sim \frac{\mathrm{Ma}}{\mathrm{Re}_{\Delta x}}. \tag{15}$$

This motivates to formulate a regularization $\omega^{\mathrm{R}}_{\{3;4;5\}} \sim \omega_{\{3;4;5\}}[1 + \cdots (\mathrm{Re}_{\Delta x}/\mathrm{Ma})]$ of the parameterized rates (6)–(8), which does not vanish in the high-Reynolds number limit. The suggested regularization employs the same cumulant expressions $\mathbf{C}_\varepsilon$ as Geier *et al.*[27] to address the individual characteristics of the regularized expression, e.g., $\mathbf{C}_{3,1} = |C_{120} + C_{102}|$, etc., yielding

$$\omega^{\mathscr{C}}_{3,1} = \omega_3(1 + \mathscr{C}_\omega|C_{120} + C_{102}|), \tag{16}$$

$$\omega_{4,1}^{\mathscr{C}} = \omega_4(1 + \mathscr{C}_\omega |C_{120} - C_{102}|), \tag{17}$$

$$\omega_{3,2}^{\mathscr{C}} = \omega_3(1 + \mathscr{C}_\omega |C_{210} + C_{012}|), \tag{18}$$

$$\omega_{4,2}^{\mathscr{C}} = \omega_4(1 + \mathscr{C}_\omega |C_{210} - C_{012}|), \tag{19}$$

$$\omega_{3,3}^{\mathscr{C}} = \omega_3(1 + \mathscr{C}_\omega |C_{201} + C_{021}|), \tag{20}$$

$$\omega_{4,3}^{\mathscr{C}} = \omega_4(1 + \mathscr{C}_\omega |C_{201} - C_{021}|), \tag{21}$$

$$\omega_5^{\mathscr{C}} = \omega_5(1 + \mathscr{C}_\omega |C_{111}|). \tag{22}$$

Mind that the cumulant expressions $\mathbf{C}_\varepsilon$ vanish in the low-Reynolds number fully resolved limit. The resolution-sensitive regularization parameter is assigned to

$$\mathscr{C}_\omega = \mathrm{Re}_{\Delta x}/(10\,\mathrm{Ma}), \tag{23}$$

which is close to $\mathrm{Re}_{\Delta x}/\left(4\sqrt{3}\,\mathrm{Ma}\right)$ obtained from (14). To further judge the regularization, a few aspects of the cumulant expressions $\mathbf{C}_\varepsilon$ are essential: (1) The different expressions are of similar characteristics and order of magnitude, (2) they are sensitive to the strain rate and increase with the strain rate value, and (3) they scale approximately linearly with the Mach number and vanish when the grid is refined. Figure 2 outlines the Mach number dependency for an exemplary cumulant expression $C_\varepsilon = |C_{210} + C_{012}|$. The figure refers to turbulent channel flow simulations at $\mathrm{Re}_\tau = 180$ and reveals a virtually linear increase in $|C_{210} + C_{012}|$ with the employed Mach number, which secures $\mathscr{C}_\omega \mathbf{C}_\varepsilon \sim \mathrm{Re}_{\Delta x}$. Mind that displayed results refer to a fairly well-resolved case with $\Delta x^+ = 7.5$, where no additional eddy viscosity is required.

C. SGS model

When attention is directed to coarse grid simulations, e.g., resolutions beyond $\Delta x^+ \geq 50$, the predictive capabilities of the regularized

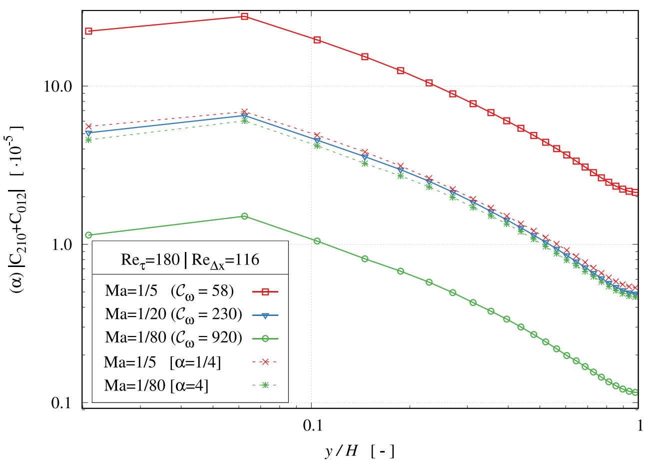

FIG. 2. Mach number dependency of the exemplary cumulant expression $|C_{210} + C_{012}|$ assessed by the simulation of a turbulent channel flow at $\mathrm{Re}_\tau = 180$. Displayed abscissa values range from the wall ($y/H = 0$) to the centerline ($y/H = 1$). All simulations were performed without explicit turbulence modeling and refer to a fixed spatial resolution ($\Delta x^+ = 7.5$, $\mathrm{Re}_{\Delta x} = 116$) in combination with three different Mach numbers $\mathrm{Ma} = \{1/5\,[\text{red}]; 1/20\,[\text{blue}]; 1/80\,[\text{green}]\}$. Dashed lines represent expressions for $\mathrm{Ma} = \{1/5; 1/80\}$ scaled with $\alpha = 1/(20\,\mathrm{Ma})$.

WP cumulant collision model in engineering shear flows reach their limits. The regularization acts upon higher-order, i.e., third-order, cumulant expressions. As demonstrated by Gehrke and Rung,[26] it addresses a fairly confined frequency range in the dissipation regime and does not affect the energy-containing and lower inertial subranges. Hence, an additional model is required to mimic the unresolved turbulent scales not addressed by the regularization. This present study utilizes a simple, heuristic eddy viscosity concept to model the subgrid-scale stresses by a dynamic Smagorinsky model.[36,37] Though eddy viscosity models of turbulence are somewhat debatable in the context of LBM,[38,39] they are often employed in practical simulations with cumulant[3,40,41] and other[42–48] collision operators. The approach alters the shear viscosity related relaxation rate[49] by a modification of the considered viscosity in (5), viz. $\omega_{1,e} = 2/(6\nu_e + 1)$. Here, $\nu_e = \nu + \nu_t$ is an effective viscosity that inheres an eddy viscosity contribution ν_t to mimic the influence of SGS stresses. The corresponding definition in SI units follows a classical approach, i.e., $\nu_{t,\mathrm{SI}} = (\mathscr{C}_\mathrm{S}\Delta x)^2_{\mathrm{SI}}\, S_{\mathrm{SI}}$, where $S_{\mathrm{SI}} = \sqrt{2S_{\alpha\beta}S_{\alpha\beta}}$ is a strain-rate measure and $\mathscr{C}_\mathrm{S}$ denotes to the scalar dynamic Smagorinsky parameter. The computation[42,43] of the scalar strain-rate measure S in non-dimensional LB units ($c_s = 1/\sqrt{3}$, $\rho_0 = 1$ incorporated) employs

$$S = \frac{\sqrt{\nu^2 + 18(\mathscr{C}_\mathrm{S}\Delta x)^2\sqrt{Q^\star}} - \nu}{6(\mathscr{C}_\mathrm{S}\Delta x)^2} \tag{24}$$

and involves the second invariant of the local nonequilibrium stress tensor $\mathbf{Q}$

$$Q^\star = \mathbf{Q}\cdot\cdot\mathbf{Q} \quad \text{with} \quad \mathbf{Q} = \sum_{ijk} \boldsymbol{e}_{ijk_\alpha}\, \boldsymbol{e}_{ijk_\beta}\, f_{ijk}^{\mathrm{neq}}. \tag{25}$$

Here, α and $\beta \in \{1,2,3\}$ denote to the components of the three-dimensional discrete velocity vector $\boldsymbol{e}_{ijk}$.

The key issue of this section is the definition of a Smagorinsky parameter $\mathscr{C}_\mathrm{S}$ using cumulant expressions. Typical values approximately fall within the range $\mathscr{C}_\mathrm{S} \in [0.05, 0.2]$, where constant values are frequently assigned to $\mathscr{C}_\mathrm{S} = 0.1$ or slightly higher when using LBM.[47,50–52] Employing an analogue ansatz as in Sec. II B 1, we assume

$$\mathscr{C}_\mathrm{S} = \mathscr{C}_{\mathrm{LES}}|C_{210} + C_{012}|. \tag{26}$$

Mind that the characteristics of the various cumulant expressions $\mathbf{C}_\varepsilon$ employed in Sec. II B 1 are fairly similar. Therefore, the selection of $|C_{210} + C_{012}|$ is deemed uncritical, and other choices would only require re-adjusting $\mathscr{C}_{\mathrm{LES}}$ along the route outlined in the remainder of this subsection. The task is to model $\mathscr{C}_{\mathrm{LES}}$, where a resolution-dependent formulation is sought, i.e., $\mathscr{C}_{\mathrm{LES}} = f(\mathrm{Ma}, \mathrm{Re}_{\Delta x})$. To this end, we first assess the interplay between $\mathscr{C}_{\mathrm{LES}}$, $|C_{210} + C_{012}|$ and Ma. Motivated by results of the regularization study displayed in Fig. 2, we again impose $\mathscr{C}_{\mathrm{LES}} \sim 1/\mathrm{Ma}$ to avoid undesired temporal resolution influences on $\mathscr{C}_\mathrm{S}$. A first heuristic closure that does not consider the spatial resolution reads $\mathscr{C}_{\mathrm{LES}} = 20/\mathrm{Ma}$. The latter was obtained from a large amount of channel and periodic hill flow[26,53] (PHF) studies to provide an orientation for an upper value of $\mathscr{C}_{\mathrm{LES}}$ and yields parameter values in the desired range $\mathscr{C}_\mathrm{S} \in [0.05, 0.2]$ as exemplified in Fig. 3 (right), which shows time-averaged contour plots for the flow over a periodic hill for two different (bulk) Reynolds numbers. Instantaneous

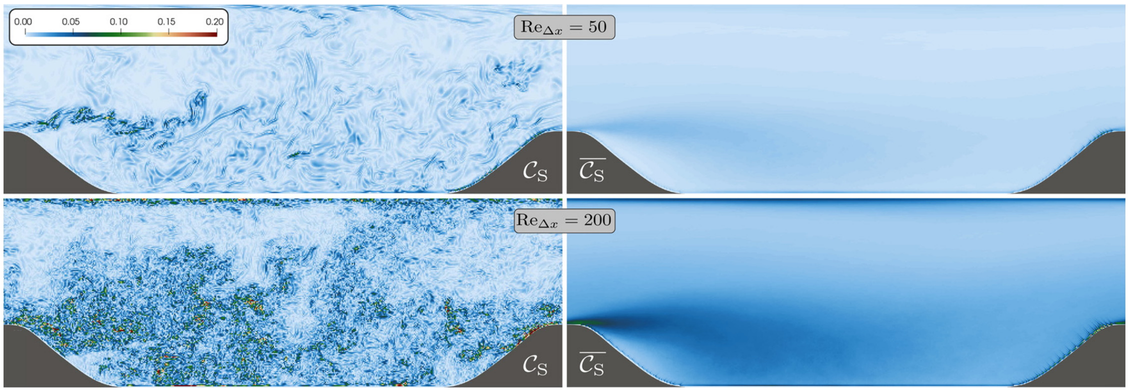

FIG. 3. Instantaneous (left) and time-averaged (right) contours of the dynamic Smagorinksy parameter $\mathscr{C}_\mathrm{S} = 20|C_{210} + C_{012}|/\mathrm{Ma}$ obtained for a periodic hill flow at $\mathrm{Re}_{\Delta x} = 50$ ($\mathrm{Re}_B = 2800$, top) and $\mathrm{Re}_{\Delta x} = 200$ ($\mathrm{Re}_B = 10\,600$, bottom) using $\mathrm{Ma} = 1/10$ with $\mathscr{C}_\omega = \{50; 200\}$ from (23).

data for $\mathscr{C}_\mathrm{S}$ are supplemented on the left side of this figure to demonstrate the dynamic structure depicting capabilities of the ansatz (26). Computations reveal resolution-dependent time-averaged maximal values in the range of $0.09\,(\Delta x^+ \approx 3, \mathrm{Re}_{\Delta x} = 50) \le \mathscr{C}_\mathrm{S} \le 0.2$ $(\Delta x^+ \approx 30, \mathrm{Re}_{\Delta x} = 750)$. It is interesting to note that, unlike many dynamic SGS approaches for Navier–Stokes simulations,[37,54] no spatial or temporal averaging of computed $\mathscr{C}_\mathrm{S}$ value is required to stabilize the simulations for the present cumulant based SGS approach, which is deemed beneficial for practical applications.

Figure 4 displays results obtained for a channel flow at $\mathrm{Re}_\tau = 550$, which serves as a reference case for the resolution-dependent formulation of $\mathscr{C}_\mathrm{LES}$ explained below. Displayed results refer to $H/\Delta x = 24$ grid points across the channel height H, which yields $\Delta x^+ = 23$ and $\mathrm{Re}_{\Delta x} = 415$. The depicted comparison involves three different Mach numbers $\mathrm{Ma} = \{1/5; 1/20; 1/80\}$ and employs the regularization (23). Figure 4(left) focuses upon the variation of $|C_{210} + C_{012}|$ with Ma for a fixed $\mathscr{C}_\mathrm{LES} = 400$. The figure reveals $|C_{210} + C_{012}| \sim \mathrm{Ma}$. Figure 4(right) employed $\mathscr{C}_\mathrm{LES} = 20/\mathrm{Ma} = \{100; 400; 1600\}$ to assess the variation of the eddy viscosity with Ma and $|C_{210} + C_{012}|$. Mind that the eddy viscosity only reaches a peak value of $\nu_t/\nu \approx 1$ at the wall nearest location of $y^+ \approx 12$ on the displayed high-Re number grid but vanishes on low-Re grids for $y^+ \to 0$ due to the vanishing cumulant expression $|C_{210} + C_{012}|$, see also Fig. 18. Figure 4(right) indicates $|C_{210} + C_{012}| \sim \mathrm{Ma}$ due to $\nu_t/\nu \sim \mathscr{C}_\mathrm{LES}\,|C_{210} + C_{012}| \approx$ constant for $\mathscr{C}_\mathrm{LES} \sim 1/\mathrm{Ma}$, and, thus, that the time-averaged cumulant expression $|C_{210} + C_{012}|$ approximately scales with $\mathscr{C}_\mathrm{LES}^{-1}$. Moreover, the influence of the regularization parameter $\mathscr{C}_\omega$ on the cumulant expression diminishes when the eddy viscosity is active, even for the low-eddy viscosity levels experienced in this case. This observation is confirmed by supplementary data using a fixed regularization value of $\mathscr{C}_\omega = 830$ added to the right graph of Fig. 4 and might support the scale-separation arguments between regularizing the high-frequency dissipation regime and turbulence modeling in the inertial regime.

Similar to the formulation of the regularization parameter $\mathscr{C}_\omega$ (23), an influence of $\mathrm{Re}_{\Delta x}$ is also sought for the Smagorinsky parameter $\mathscr{C}_\mathrm{S}$, which should ideally vanish for $\mathrm{Re}_{\Delta x} \to 0$. To this end, we analyze the spatial resolution dependent behavior of $|C_{210} + C_{012}|$, bearing in mind that $\mathscr{C}_\mathrm{LES}$ reciprocally scales with $|C_{210} + C_{012}|$. Figure 5 displays time-averaged results obtained for the turbulent channel flow at $\mathrm{Re}_\tau = 550$ and $\mathrm{Ma} = 1/10$. Displayed data were compiled for a wide range of resolutions, which reach from $H/\Delta x = 8$ lattice nodes ($\mathrm{Re}_{\Delta x} \approx 2500$, $\Delta x^+ \approx 140$) to $H/\Delta x = 96$ nodes ($\mathrm{Re}_{\Delta x} \approx 200$, $\Delta x^+ \approx 11$).

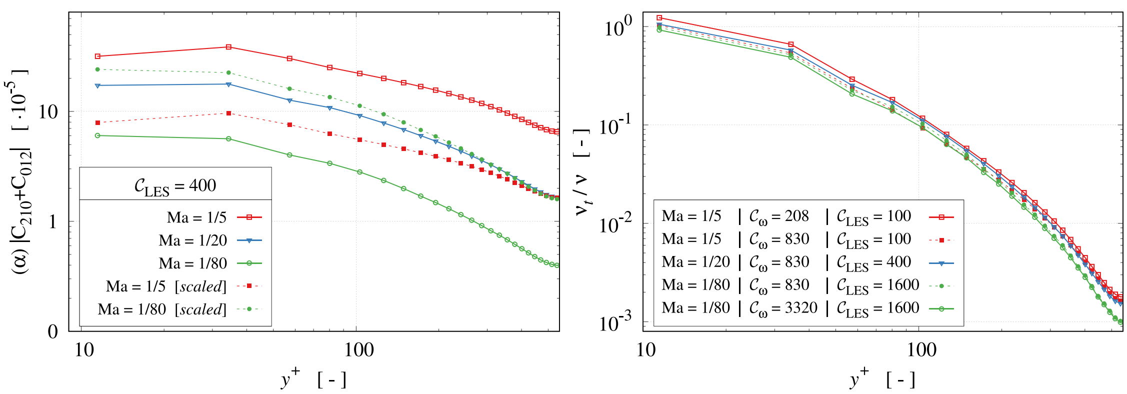

FIG. 4. Turbulent channel flow simulations at $\mathrm{Re}_\tau = 550$ resolved with $\Delta x^+ = 23$ ($\mathrm{Re}_{\Delta x} = 415$): Mach number influence on the cumulant expression $|C_{210} + C_{012}|$ using $\mathscr{C}_\mathrm{LES} = 400$ (left; dashed lines scaled by Ma) and computed eddy viscosities (right) obtained with a $\mathscr{C}_\mathrm{LES} = 20/\mathrm{Ma}$.

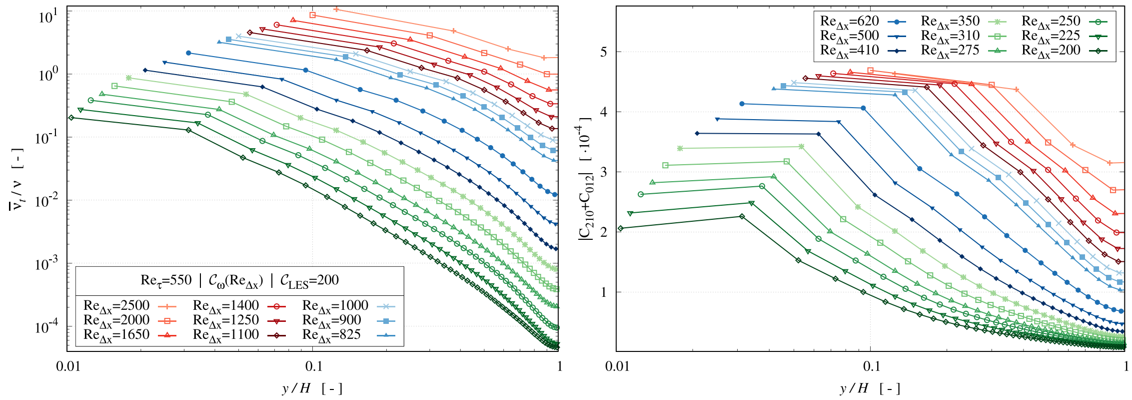

FIG. 5. Turbulent channel flow simulations at $\mathrm{Re}_\tau = 550$ and $\mathrm{Ma} = 1/10$: Grid resolution sensitivity of the time-averaged eddy viscosity (left) and the cumulant expression $|C_{210} + C_{012}|$ (right) using a range of resolutions from $H/\Delta x = 8$ to $H/\Delta x = 96$. Computations refer to $\mathscr{C}_S = 20\,|C_{210} + C_{012}|/\mathrm{Ma}$ and $\mathscr{C}_\omega = \mathrm{Re}_{\Delta x}/(10\,\mathrm{Ma})$.

A total of 18 resolutions were investigated including nine coarse grids with 8–24 nodes, three medium grids with 32–48 nodes, and six finer grids with 56–96 nodes along with the channel height. Coarse grids are incremented by two nodes, whereas medium and fine grids are incremented by eight nodes. Results were obtained from the regularization (23) and the heuristic initial guess $\mathscr{C}_{\mathrm{LES}} = 20/\mathrm{Ma} = 200$. As depicted by the right graph of Fig. 5, the cumulant expression substantially decreases when the resolution improves, in particular in the low-shear regime near the centerline, which serves as a reference location. Furthermore, a saturation of the $|C_{210} + C_{012}|$ increase is depicted for gradually coarsened grids, and the difference between near-wall and centerline values of $|C_{210} + C_{012}|$ decreases. The normalized eddy viscosity behaves similarly. However, the value range between the wall and the centerline locations spans several orders of magnitude for the fine grids.

Aiming to estimate of the scaling of $|C_{210} + C_{012}|$ with $\mathrm{Re}_{\Delta x}$, we analyze the results of these 18 resolutions for $\mathrm{Re}_\tau = 550$. Figure 6 (right) depicts the result of the regression analysis, which reveals $|C_{210} + C_{012}| \sim \mathrm{Re}_{\Delta x}^{-0.65}$.

The respective left graph shows scaled data already displayed in Fig. 5(right) and demonstrates a fairly reasonable agreement of the scaled (near) centerline values. Due to the reciprocal behavior of $\mathscr{C}_{\mathrm{LES}}$ and $|C_{210} + C_{012}|$, we assume $\mathscr{C}_{\mathrm{LES}} \sim \sqrt{\mathrm{Re}_{\Delta x}}/\mathrm{Ma}$, which employs a slightly reduced exponent of 0.5 instead of 0.65 to counteract unfavorable lower deviations from the underlying value of $20/\mathrm{Ma}$ on the finer grids. The final model reads

$$\mathscr{C}_{\mathrm{LES}} = 0.35\,\frac{\sqrt{\mathrm{Re}_{\Delta x}}}{\mathrm{Ma}}, \tag{27}$$

where the empirical parameter 0.35 follows from matching the initial guess for very coarse resolutions, i.e., $0.35\sqrt{\mathrm{Re}_{\Delta x}}/\mathrm{Ma} \approx 20/\mathrm{Ma}$ at $\mathrm{Re}_{\Delta x} \approx 3500$ and was verified with studies for $\mathrm{Re}_\tau = 550$ for a moderate ($N_H = 22$, $\mathrm{Re}_{\Delta x} = 500$) and a very coarse ($N_H = 8$, $\mathrm{Re}_{\Delta x} = 2500$) resolution. Investigations of the present study are limited to $\mathrm{Re}_{\Delta x} \le 10800$, which yields $\mathscr{C}_{\mathrm{LES}} = 36.4/\mathrm{Ma}$. One might, thus, also limit the numerator of (27), e.g., in line with the first approach $\mathscr{C}_{\mathrm{LES}} = 20/\mathrm{Ma}$ employing

$$\mathscr{C}_{\mathrm{LES}} = \min\left(20, 0.35\sqrt{\mathrm{Re}_{\Delta x}}\right)/\mathrm{Ma}. \tag{28}$$

D. Wall function

The use of a wall function, which is frequently employed in conjunction with complex flows and LBM,[55–59] is the third ingredient of

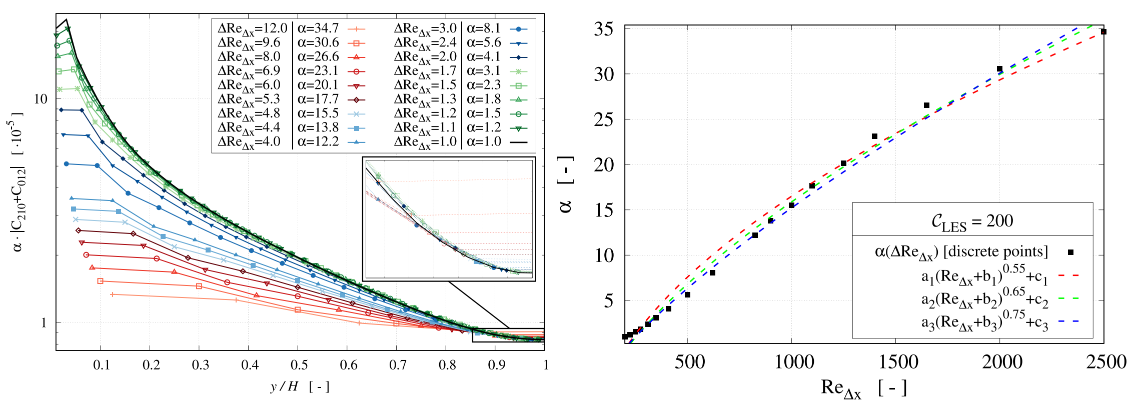

FIG. 6. Turbulent channel flow simulations at $\mathrm{Re}_\tau = 550$, $\mathrm{Ma} = 1/10$ with $\mathscr{C}_{\mathrm{LES}} = 20/\mathrm{Ma}$, and $\mathscr{C}_\omega = \mathrm{Re}_{\Delta x}/(10\mathrm{Ma})$: Resolution dependent scaling of the time averaged cumulant expression $\alpha|C_{210} + C_{012}|$ (left) using a range of resolutions from $H/\Delta x = 8$ to $H/\Delta x = 96$. The right graph depicts the evolution of the scaling factor α with the cell Reynolds number $\mathrm{Re}_{\Delta x}$ ($a_{1,2,3} = \{0.61; 0.28; 0.12\}$; $b_{1,2,3} = -\{50; 40; 30\}$; $c_{1,2,3} = -\{10; 8; 6\}$).

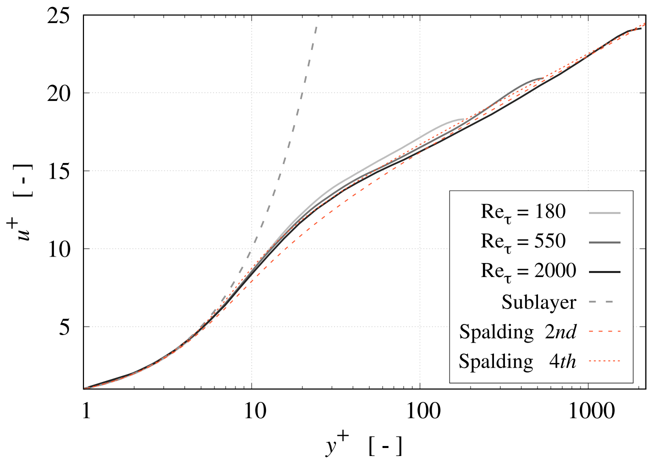

FIG. 7. Illustration of the employed wall functions obtained from piecewise polynomial reconstructions of data reported by Moser *et al.*[60] ($\mathrm{Re}_\tau = 180$) and Bernardini *et al.*[61] for $\mathrm{Re}_\tau = \{550; 2000\}$, supplemented by a second- and fourth-order Spalding law using $\kappa = 0.39$ and $B = 4.7$.

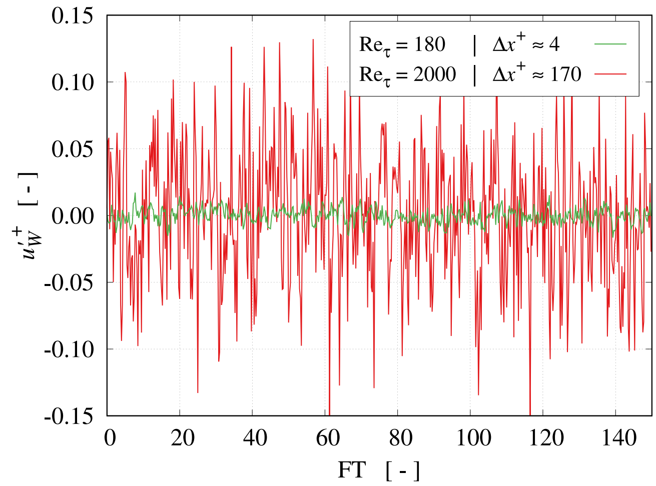

FIG. 8. Illustration of the spatially averaged instantaneous wall function behavior for a fine grid with $y_1^+ = \Delta x^+/2 \approx 2$ (green) and a coarse grid featuring $y_1^+ = \Delta x^+/2 \approx 85$ (red) simulation of a turbulent channel flow.

the present approach. The presently employed wall function refers to a recent publication of Asmuth *et al.*[41] and computes a wall velocity vector $\boldsymbol{u}_W$ that induces the desired wall shear stress τ_W obtained from a classical wall function. The merits of the method refer to its robustness and the compatibility with universal *all-resolution* wall function strategies that bridge the viscous sublayer with the buffer layer and the logarithmic region. Hence, it is readily employed to investigate a range of resolutions.

The present study utilizes a piecewise reconstruction of three non-dimensional $u^+(y^+)$ velocity profiles communicated by Moser *et al.*[60] for a lower Reynolds number of $\mathrm{Re}_\tau = 180$ and Bernardini *et al.*[61] for $\mathrm{Re}_\tau = 550$ and $\mathrm{Re}_\tau = 2000$. The distinctive friction Reynolds number follows from $\mathrm{Re}_\tau = u_\tau H/\nu_{\mathrm{SI}}$, where H denotes half the channel height, cf. Fig. 9, and $u_\tau = |\tau_W|/\rho$ refers to the friction velocity, which is computed from the magnitude of the wall-shear stress and the density. To this end, we use five consecutive segments of third-order polynomials, cf. Appendix A and Fig. 7, which support continuous functions and gradients. The employed reconstruction of $u^+(y^+)$ extracted from DNS data can be readily replaced by any similar and more general method, such as wall function approaches by Spalding,[62,63] Musker,[64] Werner and Wengle.,[65] or Shih *et al.*,[66,67] which all reconstruct the shear stress from a modeled $u^+(y^+)$ relation using the wall distance and tangential velocity at a wall-adjacent node, and usually agree with the present data, cf. Fig. 7.

Though the wall function approach originates from an averaged framework, the solid boundary treatment is performed for the local instantaneous velocities, which is an alternative to spatial[68] or temporal[69] averaging of entry values and is often used in more complex flows.[70–72] Mind that temporal exponential filtering[69] did not indicate substantial result changes and is, thus, discarded for the sake of brevity. Figure 8 summarizes the behavior of the instantaneous wall function method for a fine and a coarse grid channel flow example addressed in the results Sec. V and, indeed, indicates negligible to minor temporal fluctuations of the non-dimensional streamwise wall velocity component.

The method involves the following algorithmic sequence:

(i) Apply the boundary condition of Yu *et al.*[73] to receive the unknown PDFs reflected from the wall to the *first* fluid layer.
(ii) Compute the momentum exchange force $\boldsymbol{F}^{\mathrm{MEM}\|}$ between the solid and *first* fluid node in the wall-tangential ($\|$) direction from the method of Bouzidi *et al.*[74]

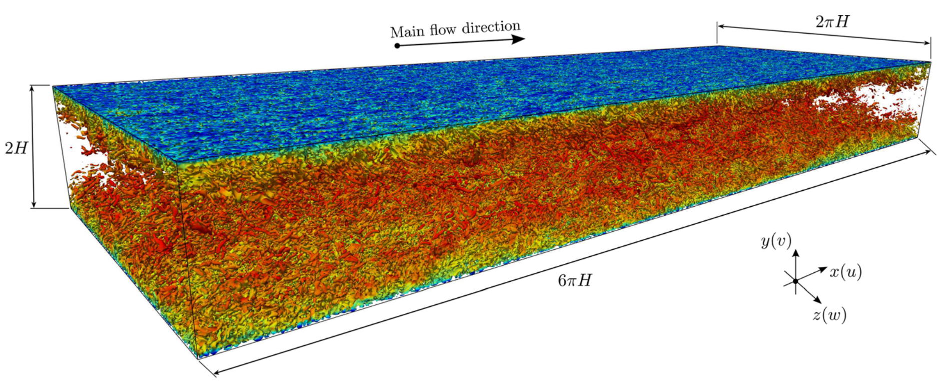

FIG. 9. Illustration of the employed channel flow domain, where the wall normal direction agrees with the *y*-coordinate. The outline is supplemented by *Q*-criterion isosurfaces colored by the streamwise velocity (u) obtained from a fine grid ($N_H = 48$) simulation for $\mathrm{Re}_\tau = 2000$.

(iii) Extract the wall-tangential magnitude of the (instantaneous) velocity vector $u_2^{\parallel} = |\boldsymbol{u}_{2^{\parallel}}|$ at the *second* fluid layer, i.e., the wall function reference location.
(iv) Initialize the friction velocity u_τ, e.g., based on the explicit power law of Wilhelm *et al.*[75] and iterate u_τ based on the $u_2^+(y_2^+, u_2^{\parallel})$ wall function (Fig. 7):
 - Compute $y_2^+ = (u_\tau y_2)/\nu$ at the reference location with $y_2 = 3/2\Delta x$ due to the underlying grid layout.
 - Update friction velocity via $u_\tau = u_2^{\parallel}/u_2^+(y_2^+)$.
 - Proceed until convergence criterion $|y_{2,n+1}^+ - y_{2,n}^+| < 1/200$ is fulfilled.
(v) Assign the wall shear stress to $\tau_W = u_\tau^2\,\rho$ and compute related shear force $\boldsymbol{F}^{\parallel} = \tau_W\,\Delta x^2(\boldsymbol{u}_1^{\parallel}/u_1^{\parallel})$ considering the sign of the tangential velocity $\boldsymbol{u}_1^{\parallel}$ at the *first* node.
(vi) Assign the difference $\boldsymbol{F}^{\parallel} - \boldsymbol{F}^{\mathrm{MEM}\parallel}$ to the force $\boldsymbol{F}^{\boldsymbol{u}_W}$ contribution to be applied via a wall velocity $\boldsymbol{u}_W$. For a y-aligned plane wall normal, this reads[41] $\boldsymbol{u}_W = -\frac{9c_s^2}{\rho}\frac{\Delta t^2}{\Delta x^4}\,\boldsymbol{F}^{\boldsymbol{u}_W}(1, 1/3, 1)^\top$.
(vii) Introduce wall velocity $\boldsymbol{u}_W$ into the *first* fluid layer PDFs (i), e.g., via PDF($\boldsymbol{u}$) relation given in Chen *et al.*[76]

E. Suggested model

The suggested cumulant collision operator employs the parameterization of the third-order relaxation rates (6)–(8), which follows from Geier *et al.*[27] together with $\omega_2 = 1$. The parameterization is regularized using (16)–(22) together with the resolution-sensitive regularization parameter $\mathscr{C}_\omega = \mathrm{Re}_{\Delta x}/(10\,\mathrm{Ma})$ from (23).

The model is augmented by a dynamic SGS replacing ω_1 by an effective relaxation rate $\omega_{1,e}$. Using LB units, this reads

$$\omega_1 \leftarrow \omega_{1,e} = \frac{2}{\left[6\left(\nu + \mathscr{C}_S^2\,S\right) + 1\right]} \tag{29}$$

due to $\nu_t = \mathscr{C}_S^2 S$, and the non-dimensional strain-rate measure S follows from (24). The Smagorinsky parameter $\mathscr{C}_S$ is computed from the cumulant expression $\mathscr{C}_S = \mathscr{C}_{\mathrm{LES}}|C_{210} + C_{012}|$ and a resolution-sensitive coefficient, which reads $\mathscr{C}_{\mathrm{LES}} = 0.35\sqrt{\mathrm{Re}_{\Delta x}}/\mathrm{Ma}$ in line with (27).

A note of caution is necessary as regards the influence of the SGS on the parameterized cumulant model. According to the parameterization (6)–(8), the relaxation rates $\omega_{\{3,4,5\}}$ depend on ω_1. Hence, two options exist to compute $\omega_{\{3,4,5\}}$ in combination with the dynamic eddy viscosity: one using the SGS-modified $\omega_{1,e}$ and one using the unmodified ω_1. We employed the unmodified ω_1 in conjunction with the parameterization during the present study. Related differences were examined and deemed negligible for the finer grids. For the coarser grids ($\Delta x^+ \geq 30$), minor deviations, which are more pronounced for the Reynolds-stresses than for the mean velocity, are observed for the two to three wall-nearest grid points.

The computational model employs the wall function outlined in Sec. II D, which supports all (near-wall) resolutions.

III. TEST CASE AND SCALING

Section III describes the considered plane turbulent channel flow case and introduces the underlying grid layout and domain size. Moreover, we outline the corresponding correlation between physical (subscript SI) and non-dimensional LB units (no subscript).

A. Test case

Turbulent channel flow studies of the present paper are performed for four Reynolds numbers $\mathrm{Re}_\tau = \{180; 550; 2000; 5200\}$. The flow is computationally driven by a steady, homogeneous axial pressure gradient $\partial p/\partial x$, which is imposed as a body force acting on every fluid node via $F_{x,\mathrm{SI}} = [(\partial p/\partial x)\,\Delta x^3]_{\mathrm{SI}}$. The pressure gradient is supposed to balance the mean shear load, which, in turn, is assumed to display a linear variation along the vertical coordinate, viz.,

$$\left(\frac{\partial p}{\partial x}\right)_{\mathrm{SI}} = \left(\frac{\partial \tau}{\partial y}\right)_{\mathrm{SI}} = \left(\frac{|\tau_W|}{H}\right)_{\mathrm{SI}} = \mathrm{Re}_\tau^2\left(\frac{\nu^2\rho}{H^3}\right)_{\mathrm{SI}}, \tag{30}$$

where H refers to the channel half height. Hence, the employed body force is rigidly linked to the prescribed friction Reynolds number.

B. Spatial domain

Figure 9 illustrates the spatial domain, supplemented by isosurface plots of the Q-criterion[77] compiled for $\mathrm{Re}_\tau = 2000$. Results included in this paper address three resolutions for each considered Re_τ featuring $N_H = \{12; 24; 48\}$ lattice nodes along the channel half height H. Table I summarizes the details of the employed grids. The domain size reads $6\pi H$ in streamwise (x), $2\pi H$ in spanwise (z), and $2H$ in wall-normal directions (y). It aims to accommodate the largest expected turbulent structures combined with periodic continuations in both streamwise and spanwise directions. All nine computations employ an isotropic, homogeneous spatial resolution. In the wall-normal direction, $N_y = 2N_H + 2$ applies, attributed to two solid boundary nodes, which yield $y_1 = \Delta x/2$.

C. Scaling

The present grid layout reads $\Delta x_{\mathrm{SI}} = H/N_H$ (m), which directly results in a length-scale ratio $\Lambda_x = \Delta x_{\mathrm{SI}}/\Delta x = H/N_H$. Since the investigated flow is characterized by an *inner* Reynolds number (Re_τ), the related *outer* bulk Reynolds number (Re_B) is compiled from Dean's correlation,[78]

$$\mathrm{Re}_B = \left(\frac{H\,u_B}{\nu}\right)_{\mathrm{SI}} = \left(\frac{8}{0.073}\right)^{4/7}\frac{\mathrm{Re}_\tau^{8/7}}{2}, \quad u_{B,\mathrm{SI}} = \frac{1}{H}\int_0^H u\,\mathrm{d}y. \tag{31}$$

Using (31), the four investigated friction Reynolds numbers yield $\mathrm{Re}_B \approx \{2750; 9900; 43\,900; 129200\}$. For a given geometry and known fluid properties, e.g., $H = 0.05$m and $\nu_{\mathrm{SI}} = 1.5\times10^{-5}\mathrm{m}^2/\mathrm{s}$, one obtains the bulk velocity u_{SI} compatible to the Reynolds number $\mathrm{Re}_B(\mathrm{Re}_\tau)$.

The time step of the explicit time integration scheme refers to $\Delta t_{\mathrm{SI}} = \Delta x_{\mathrm{SI}}/\Lambda_u$ (s), where Λ_u (m/s) is the velocity scaling ratio $u_{B,\mathrm{SI}}/u_B$. The non-dimensional bulk velocity u_B approximately scales with the mean centerline velocity via $u_B \approx u_C/1.16$ (-). The latter is

TABLE I. Investigated grids and related discrete time steps per flow-through time (FT) at Ma = 1/20.

N_H	$N_x \times N_y \times N_z$	Total grid size	FT (rounded)
12	227 × 26 × 76	448 552	9120
24	453 × 50 × 152	3 442 800	18 240
48	906 × 98 × 303	26 902 764	36 480

an approximation of the mean maximum velocity and, therefore, relates to the user-defined Mach number, viz. $u_C = \mathrm{Ma}/\sqrt{3}$ (-). The system is closed by the non-dimensional kinematic viscosity in LB units to ensure Reynolds similarity, viz.,

$$\nu = \frac{\mathrm{Ma}\, N_H}{1.16\,\sqrt{3}\,\mathrm{Re}_B} \quad [-]. \tag{32}$$

Using $\rho = \rho_0 = 1$ and $\Delta x^3 = 1$, the non-dimensional viscosity is also used to compute a non-dimensional body force $F_x = \nu^2\,\mathrm{Re}_\tau^2/N_H^3$ that drives the flow, cf. (30). Mind that all simulations depicted in the results Sec. V were performed with a Mach number of $\mathrm{Ma} = 1/20$.

To judge the resolution characteristics, the dimensionless wall distance Δx^+ and the local cell Reynolds number are utilized. Using LB units, these inner and outer measures read

$$\Delta x^+ = \left(\frac{u_\tau\,\Delta x}{\nu}\right) = u_\tau/\nu \equiv \mathrm{Re}_\tau/N_H \quad [-], \tag{33}$$

$$\mathrm{Re}_{\Delta x} = \left(\frac{u_B\,\Delta x}{\nu}\right) = u_B/\nu \equiv \mathrm{Re}_B/N_H \quad [-]. \tag{34}$$

Moreover, we also use the conventional flow descriptors for the inner boundary layer, i.e., $u^+ = u/u_\tau$ and $y^+ = y\,u_\tau/\nu$. It is again noted that the non-dimensional wall distance of the first wall-adjacent node yields $y_1^+ = \Delta x^+/2$ due to the underlying Cartesian grid alignment.

D. Time domain

The non-dimensional flow-through time, based on the longitudinal extension of the domain N_x, the bulk velocity u_B (31), and the discrete unit time step $\Delta t = 1$ read

$$\mathrm{FT} = \frac{N_x}{u_B\,\Delta t} \overset{(31),(32)}{=} 6.96\,\sqrt{3}\pi\,\frac{N_H}{\mathrm{Ma}} \approx 38\,\frac{N_H}{\mathrm{Ma}} \quad [-]. \tag{35}$$

The flow-through time quantifies the average number of time steps a particle needs to pass the domain once and serves as a reference time scale.

The statistical convergence of the evaluated flow quantities, i.e., the mean velocity, the Reynolds stresses, and the two-point correlations is ensured by comprehensive prior verification studies on a reliable data processing strategy, see also Sec. IV. The data processing sequence commences with an initial transient phase of 50 FT. This is followed by 50 FT to compute time-averaged velocity values $\bar{\boldsymbol{u}}$. The Reynolds stress tensor $\bar{\mathbf{R}}(\bar{\boldsymbol{u}}, \boldsymbol{u})$ and the two-point correlations $R_\vartheta^{\{x,z\}}(\bar{\boldsymbol{u}}, \boldsymbol{u})$ are obtained during the subsequent 100 FT. Thus, the duration of each simulation refers to 200 FT. Further details of the data processing method are outlined in Sec. IV.

Table II provides an overview of the computed test matrix. The LB viscosity ν spans two orders of magnitude, while the grid resolution is bounded by $4 \leq \Delta x^+ \leq 430$ and $60 \leq \mathrm{Re}_{\Delta x} \leq 10800$. The last column of Table II verifies the validity of Dean's correlation (31), and the observed deviation of approximately $\pm 4\%$ is deemed sufficiently small. To this end, the simulation input comprises *(a)* a target Re_τ, *(b)* an assumed correlation between Re_τ and Re_B obtained from Dean (31), and *(c)* its hypothesized relation to a prescribed Mach number given by $\mathrm{Re}_B\,\nu/N_H = \mathrm{Ma}/(1.16\sqrt{3})$. The latter relation is used to compute the viscosity ν, which, in turn, is used to obtain a reference friction velocity $u_\tau = \mathrm{Re}_\tau\,\nu/N_H$. Minor deviations of the displayed normalized properties in Sec. V, e.g., $\boldsymbol{u}^+ = \bar{\boldsymbol{u}}/u_\tau$ or $\mathbf{R}^+ = \bar{\mathbf{R}}/u_\tau^2$, are attributed to small inaccuracies of the assumed correlations and might be reduced by alternative assessments of u_τ.

TABLE II. Considered twelve test cases, including their respective spatial resolution parameters N_H, Δx^+, $\mathrm{Re}_{\Delta x}$, and kinematic viscosity in LB units ($\mathrm{Ma} = 1/20$). The deviation of the current (c) to the targeted (t) bulk Reynolds number $\{[\mathrm{Re}_{B,c}/\mathrm{Re}_{B,t} - 1] \cdot 100\ (\%)\}$ is tabulated to verify Dean's[78] correlation.

Re_τ	N_H	ν_{LB}	Δx^+ (Re_τ/N_H)	$\mathrm{Re}_{\Delta x}$ (Re_B/N_H)	Re_B dev. (%)
180	48	4.32×10^{-04}	3.8	58	+2.6
	24	2.16×10^{-04}	7.5	115	−0.5
	12	1.08×10^{-04}	15.0	230	+3.2
550	48	1.20×10^{-04}	11.5	208	+3.7
	24	6.02×10^{-05}	22.9	415	+2.1
	12	3.01×10^{-05}	45.8	830	+0.8
2000	48	2.72×10^{-05}	42.1	915	−2.6
	24	1.36×10^{-05}	84.3	1830	+0.1
	12	6.80×10^{-06}	168.5	3660	−3.3
5200	48	9.25×10^{-06}	108.3	2690	− 2.4
	24	4.62×10^{-06}	216.7	5380	−2.6
	12	2.31×10^{-06}	433.3	10760	−2.3

IV. DATA RECORDING AND DATA PROCESSING

This section includes a synopsis of data processing aspects. Statistical averages of $\bar{\boldsymbol{u}}$ and $\bar{\mathbf{R}}$ are extracted from time averaged data in the centered y-z plane located at $x/H = 3\pi$. A major share of the data displayed in Sec. V refers to profiles along the vertical direction (y). To this end, the time-averaged data at $x/H = 3\pi$ is spatially averaged in the spanwise direction (z), though the mean's ergodic nature virtually reveals any differences between the different time-averaged profiles and the space–time-averaged profile.

Temporal-averaged two-point correlations rest upon entire, wall-parallel (x-z) data planes located at fixed wall distances (y = const.). The data planes are subsequently condensed to the displayed one-dimensional data in the streamwise (x) or spanwise (z) directions as outlined in Sec. IV C.

A. Shear stress computation

According to Pasquali *et al.*,[24] a second-order representation of the shear stress in a laminar plane channel flow reads

$$\tau_{xy} = -3\,C_{101}\omega_1\,\nu, \tag{36}$$

where the cumulant subscripts refer to $i[x] = 1$, $j[z] = 0$ and $k[y] = 1$, owing to the orientation of the wall normal and the primal flow in the present case, cf. Figs. 1 and 9. To enable an in-depth analysis of distinct contributions, the total shear stress (subscript tot) along the x-y-plane is separated by

$$\begin{aligned} \tau_{\mathrm{tot}} &= \tau_{\mathrm{res}} + \tau_{\mathrm{vis}} + \tau_{\mathrm{mod}} \\ &= -\left(\rho\,\overline{u'v'} + 3\,C_{101}\,\omega_{1,e}(\nu + \nu_t)\right), \end{aligned} \tag{37}$$

where the subscript xy to mark the in-plane orientation is omitted in the remainder for the sake of brevity. The contributions correspond to the resolved (res) stresses and a combination of viscous (vis) and modeled (mod) stresses. The latter two involve an effective relaxation rate $\omega_{1,e}$ due to the employed Boussinesq viscosity concept, cf. Sec. II C and (29).

B. Turbulence anisotropy

The structure of the turbulence field is analyzed using the normalized (resolved) Reynolds-stress $\bar{\mathbf{R}}$ tensor involving the traceless (non-dimensional) Reynolds stress anisotropy $\mathbf{A}$ tensor defined as

$$\mathbf{A} = \frac{\bar{\mathbf{R}}}{2k} - \frac{\mathbf{I}}{3}. \tag{38}$$

Herein, k denotes the turbulent kinetic energy (TKE) defined by half the trace of the Reynolds stress tensor and $\mathbf{I}$ is the identity tensor. For an improved presentation, the evaluation refers to barycentric (B) coordinates introduced by Banerjee *et al.*[79] To this end, invariants of (38) are observed in two dimensions $(x, y)_B$ defined by

$$x_B = \Lambda_1 - \Lambda_2 + \frac{3}{2}\Lambda_3 + \frac{1}{2}, \quad y_B = \frac{\sqrt{27}}{2}\Lambda_3 + \frac{\sqrt{3}}{2}, \tag{39}$$

where Λ_i denotes the eigenvalues of $\bar{\mathbf{R}}$ sorted in descending order.

C. Two-point correlations and energy spectra

To analyze the results in greater detail and verify the adequacy of the considered domain size, one-dimensional two-point correlations $R_{\vartheta}^{x[z]}$ (m^2/s^2) were compiled in streamwise (superscript x) and spanwise (superscript z) directions for selected wall-distances (labeled Θ) employing space-time averaged line probes. Attention is confined to normal stress components, hence $\vartheta = \{\overline{u'u'}; \overline{v'v'}; \overline{w'w'}\}$. Four wall distances are investigated featuring $\Theta = y_{\mathrm{SI}}/H = (0.1; 0.25; 0.5; 1)$. The latter refer to the following set of discrete lattice nodes N_y for the three grids,

$$N_y(\Theta, N_H) = \begin{cases} \{1;\ 3;\ 6; 12\}, & N_H = 12, \\ \{2;\ 6; 12; 24\}, & N_H = 24, \\ \{4; 12; 24; 48\}, & N_H = 48, \end{cases} \tag{40}$$

where the index starts from 0, i.e., the solid boundary node. Note that no interpolation is applied for the near-wall location $y_{\mathrm{SI}}/H = 0.1$, which strictly speaking points to $\{1.2, 2.4, 4.8\}\,\Delta x$ on the three grids, and the assignment refers to the lower neighbor. This impairs an inter-grid comparison at the near-wall location $\Theta = 0.1$, as indicated by the different buffer-layer locations outlined in Table III, which states the y^+_Θ values as a function of N_H and Re_τ. Since the $\Theta = 0.1$ plane is extracted at the first (second) fluid node of the coarse (medium) grid, one expects the location to be affected by wall function influences. Wall function concepts usually refer to averaged flow properties, and a wall function generally suppresses turbulent dynamics. Therefore, results of the $\Theta = 0.1$ plane are assumed to show more substantial deviations from DNS data for all simulations that do not resolve the viscous sublayer at $\mathrm{Re}_\tau = 550$ and $\mathrm{Re}_\tau = 2000$.

The two-point correlations are computed in the entire x-z planes. However, evaluations rest upon axially parallel lines in stream- and spanwise directions controlled by a running index $\varepsilon = \{0; N_{x[z]} - 1\}$,

$$R^x_{\overline{u'u'}}(x, z_\varepsilon, \Theta) = \overline{u'(x = 0, z_\varepsilon, \Theta)\, u'(x, z_\varepsilon, \Theta)}, \tag{41}$$

$$R^z_{\overline{u'u'}}(x_\varepsilon, z, \Theta) = \overline{u'(x_\varepsilon, z = 0, \Theta)\, u'(x_\varepsilon, z, \Theta)} \tag{42}$$

TABLE III. Resulting $y^+_\Theta = y^+(N_H, \mathrm{Re}_\tau)$ values at the considered wall distances $\Theta = y_{\mathrm{SI}}/H$ for computing two-point correlations and energy spectra.

Θ	N_H	Re_τ	y^+_Θ	Θ	N_H	Re_τ	y^+_Θ
0.1	12	180	7	0.5	12	180	82
		550	23			550	252
		2000	84			2000	927
	24	180	11		24	180	86
		550	34			550	264
		2000	126			2000	969
	48	180	13		48	180	88
		550	40			550	269
		2000	147			2000	990
0.25	12	180	37	1	12	180	172
		550	115			550	527
		2000	421			2000	1938
	24	180	41		24	180	176
		550	126			550	539
		2000	463			2000	1980
	48	180	43		48	180	178
		550	132			550	544
		2000	484			2000	2001

exemplary depicted for the $\overline{u'u'}$ component. The displayed one-dimensional two-point correlation follows from in-plane spatial averages, viz.,

$$R_{\vartheta}^{x[z]}(x[z], \Theta) = 1/N_{z[x]} \sum_{\varepsilon=0}^{N_{z[x]}-1} R_{\vartheta}^{x[z]}(x[x_\varepsilon], z_\varepsilon[z], \Theta). \tag{43}$$

Related one-dimensional energy spectra $E_{\vartheta}^{x[z]}(k_{x[z]})$ (m^3/s^2) computed from averaged two-point correlations are used to assess the energy distribution along the resolved scales. Here, $k_{x[z]}$ (1/m) denotes the wave number, whereby low values correspond to large scales. The energy spectra are obtained from discrete Fourier transformation[80] (DFT) and require an adequate processing of the averaged two-point correlation (43), particularly a symmetric input. Figure 10 illustrates the adopted four-step symmetrization approach for an example with five (left) and four (right) input points.

First, the global maximum (zeroth) element ($x = 0$) is assigned to the mid value (0), which remains unchanged. Subsequently, an unweighted mean is computed for $x[z] > 0$ via

$$R(x[z]) = \frac{R(x[z] + R(N_{x[z]} - x[z])}{2} \quad x[z] = \{1; \ldots; \varsigma\} \tag{44}$$

with $\varsigma = (N_{x[z]} - 1)/2$ (odd) and $\varsigma = N_{x[z]}/2 - 1$ (even) as indicated by (2) in Fig. 10 (sub and superscript omitted for clarity). Averaging eliminates (numerical) deviations of the actually symmetrical R shape, which should not occur due to the assumed stream- and spanwise periodicity. Subsequently, the values are shifted (3) to the right-hand side of the center. Intended symmetric correlations follow from data mirroring (4). Thus, the length ($N_{x[z]}$) of $R_{\vartheta}^{x[z]}$ is incremented by one for even input elements. The orange dashed line in Fig. 10, covering

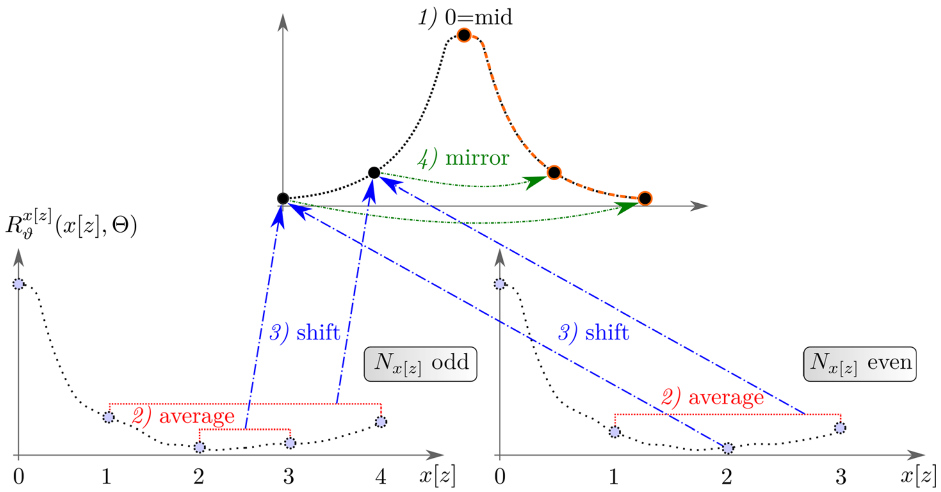

FIG. 10. Employed $R_\vartheta^{x[z]}$ symmetrization algorithm for an even (odd) number of input data. Points along dotted lines in the bottom figures represent 1D two-point correlations defined by (43). The resulting DFT input is illustrated by the closed black circles in the top figure.

the half pathway starting from the global maximum, exemplary represents the two-point correlation data shown in the results section, where the trajectories are additionally normalized using their maxima.

The discrete energy contributions $E_\vartheta^{x[z]}(k_{x[z]})$ per wave number $k_{x[z]} = 2\pi\, x[z]/N_{x[z]}$ correspond to the magnitude of the computed Fourier coefficients. In order to reduce oscillations, the symmetric DFT input (R) is filtered[81] using a von Hann window $(1/2 - \cos(2\pi\, x[z]/N_{x[z]})/2)$. Due to the odd number of real input elements in the present study, we obtain $N_B = (N_{x[z]} + 1)/2$ [bin indexing: $[0 : (N_{x[z]} - 1)/2]$] DFT bins attributed to conjugate (Hermitia) symmetry.

The representation is non-dimensionalized by means of $E^+ = E/(u_\tau^2\, N_H)$ plotted over $k^+ = k\, N_H$. The first bin with the zero wave number contribution is not displayed, and a cutoff $k_c = 0.9\, N_B$ is applied to all spectra. To suppress strong oscillations in the high wave number regime, the streamwise spectra are additionally truncated as follows. The conditions are (i) $k_c > 0.4\, N_B$, (ii) positive E gradient, and (iii) $E(k)/E(k-1) > 3/2$ to avoid excessive sharp cutting for minor gradients.

Moreover, integral lengths scales are computed from the two-point correlations via

$$\lambda_{x[z]}^{+}(y_\Theta) = \frac{1}{u_\tau\, \nu} \int_0^{\mathrm{r}} R_\vartheta^{x[z]} \mathrm{d}x[\mathrm{d}z] \overset{y_\Theta = y^+}{=} \int_0^{\mathrm{r}} R_\vartheta^{x[z],+} \mathrm{d}x^+[\mathrm{d}z^+] \tag{45}$$

to assess the computed structures and the sensitivity to resolution aspects. To avoid cancelation of positive and negative values, the integral lengths are evaluated from their (positive) origin to the first root (r) of their argument.

V. RESULTS

Results obtained on the different grids are assigned to a particular color. Green indicates fine grid results ($N_H = 48$), blue denotes to medium grid results ($N_H = 24$), and red refers to coarse grid solutions ($N_H = 12$). Black lines refer to the respective reference data reported by Kim *et al.*[82] and Moser *et al.*[60] for $\mathrm{Re}_\tau = 180$ as well as Bernardini *et al.*[61] and Lee and Moser.[83] for the higher Reynolds numbers. Note that the simulations of Lee and Moser.[83] and Bernardini *et al.*[61] to some extent cover virtually the same Reynolds numbers, and the respective data for these Reynolds number basically agree. Hence, the remainder of the section simply distinguishes between $\mathrm{Re}_\tau = \{180, 550, 2000\}$ and $\mathrm{Re}_\tau = 5200$ is only referred to in Sec. V G. Two-point correlations and spectra computed for $\mathrm{Re}_\tau = 550$ are compared to DNS reference data[60] for $\mathrm{Re}_\tau = 590$.

A. Domain size and periodicity conditions

The employed box domain depicted in Fig. 9 agrees with previous studies of Bernardini *et al.*[61] Assuming periodic boundary conditions, an insufficiently small domain size might affect the credibility of turbulence statistics due to the large correlation lengths, as, for example, demonstrated in Moser *et al.*[60] The suitability of the present domain/periodicity condition combination is demonstrated in Figs. 11 and 12 by exemplary two-point correlations and energy spectra of the normal stresses in streamwise and spanwise directions for the most challenging large Reynolds number $\mathrm{Re}_\tau = 2000$. Displayed correlations refer to fine grid results ($N_H = 48$) for the mid height position ($y/H = 0.5$) and descent all to sufficiently small values. Furthermore, the minimum spanwise correlation for the streamwise component displays the frequently observed half-streak spacing at this wall distance.

The corresponding energy densities shown in Fig. 12 drop with an increasing slope by approximately five[3] orders of magnitude between the low and the high wave numbers in the streamwise (spanwise) direction.

B. Mean velocity

Figure 13 depicts profiles of the non-dimensional mean primal velocity $u^+(y^+)$ obtained for the three considered Reynolds numbers on the three grids. Overall, results are deemed to be quite accurate and display a surprisingly small sensitivity to the grid resolution.

In conjunction with the smallest Reynolds number $\mathrm{Re}_\tau = 180$ illustrated in the left graph of Fig. 13, the wall adjacent fluid node is still inside the viscous sublayer (fine, medium grid) or the buffer layer (coarse grid). Hence, only a weak deviation from the no slip velocity is

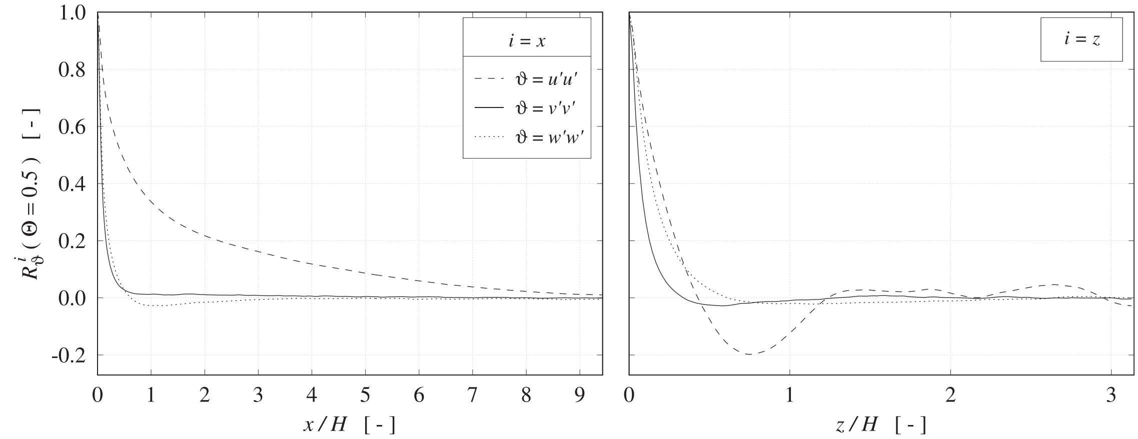

FIG. 11. Stream- (left) and spanwise (right) normalized two-point correlations obtained from the fine grid ($N_H = 48$) for $\mathrm{Re}_\tau = 2000$ at $\Theta = 0.5$.

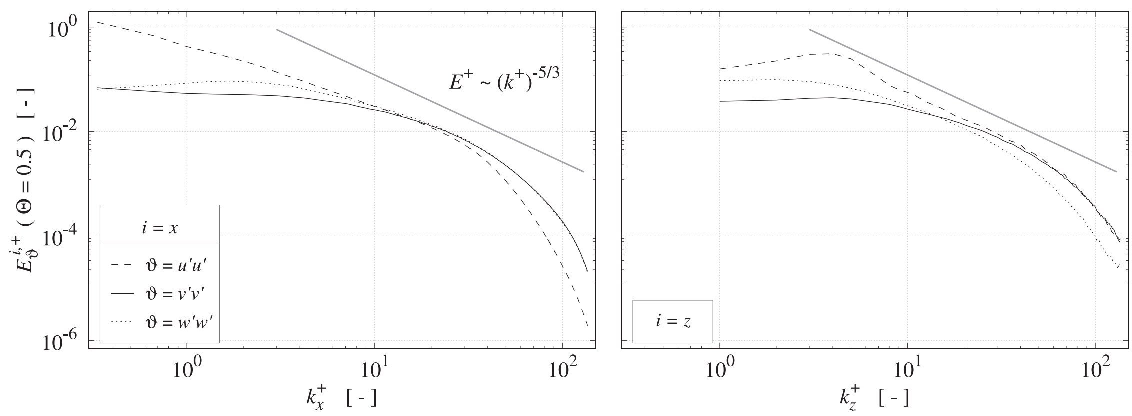

FIG. 12. Stream- (left) and spanwise (right) normalized turbulent energy spectra obtained from the fine grid ($N_H = 48$) for $\mathrm{Re}_\tau = 2000$ at $\Theta = 0.5$. The $\overline{u'u'}$-component in the spanwise direction (dashed, right) is smoothed by a centered, unweighted three-point moving average filter applied for $k_z^+ > 0.7$. Additionally, the $E^+ \sim (k^+)^{-5/3}$ proportionality of the inertial range is displayed.

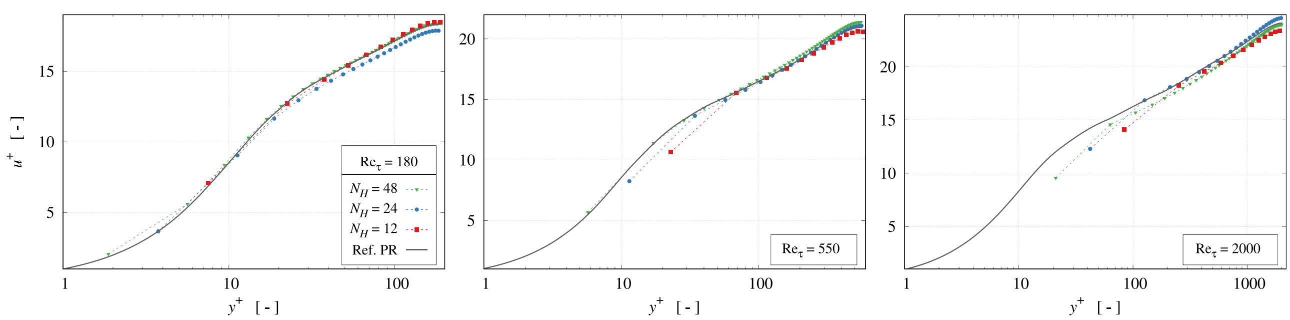

FIG. 13. Non-dimensional mean velocity profiles for the three considered Re_τ in comparison with the polynomial reconstruction (Ref. PR) of reference data.[60,61]

observed in Table IV, which outlines the x-component u_W of the wall velocity vector as described in Sec. II D (vii) and Fig. 8. The table also indicates that the respective variance increases when the resolution deteriorates but always remains small.

With attention directed to the two larger Reynolds numbers, wall function influences increase in line with an increase in wall velocity u_W. In such situations, deficiencies are observed in the vicinity of the first and second interior grid nodes in Fig. 13 (center, right). They are attributed to an *overshoot* phenomenon[41,84] induced by small eddy viscosity levels predicted at the very near-wall fluid node(s). This is due to the wall function being afflicted with reduced turbulent dynamics. The missing dynamics have an adverse effect on the present SGS

TABLE IV. Temporal mean value ($\bar{u}_W^+$) and variance ($\sigma^2_{\bar{u}_W^+}$) of the non-dimensional streamwise wall velocity component.

Re_τ	N_H	$\bar{u}_W^+$	$\sigma^2_{\bar{u}_W^+}$ (10^{-3})
180	48	0.108	0.034
	24	0.056	0.785
	12	0.665	1.365
550	48	0.246	0.205
	24	0.707	0.497
	12	2.076	2.386
2000	48	1.279	0.526
	24	3.362	0.913
	12	5.151	2.457

model that operates with third-order cumulant expressions, which are dampened by wall function influences.

However, except for the over-predicted velocity gradients at the wall-nearest nodes, the mean velocity profiles display remarkable agreement with the logarithmic layer, even for the large Reynolds number, where the resolution is decreased to $\Delta x^+ = 170$. The biggest discrepancy of the computed wall shear stress is observed for $\mathrm{Re}_\tau = 2000$ on the fine grid, where the prescribed wall shear is under-predicted by approximately 3%. Mind that normalizations employ a prescribed reference u_τ in line with Sec. III D. Moreover, minor deviations occur in the wake regime. Here, the bulk velocity deviation (Re_B dev.) might explained by a small mismatch of the employed correlations, cf. Table II.

C. Total shear, resolved, and modeled Reynolds shear stress

The overshoot phenomenon mentioned above is better understood when looking at the Reynolds-shear stresses and the total shear. Figure 14 indicates reasonable agreement of the normalized total shear stress $\tau_{\mathrm{tot}} = \tau_{\mathrm{SI,tot}}/|\tau_W|$ with a non-dimensional linear distribution $\tau_{lin} = 1 - y_{\mathrm{SI}}/H$, disregarding the Reynolds number or the employed resolution. Deviations increase with the Reynolds number but remain approximately constant along the abscissa, indicating a mismatch of the slope by mostly 5%. Mind that the linear distribution vanishes at $y/H = 1$, which impairs the evaluation of relative differences close to the centerline.

Profiles of the individual normalized shear stress components, comprising the modeled SGS, viscous, and resolved parts, are displayed in Fig. 15. It is observed that the viscous contributions obtained with different grids for specific Reynolds numbers (solid lines) agree apparently well with each other for $\mathrm{Re}_\tau = 180$, i.e., they all snap on the green fine grid curve. This is not necessarily the case for the other Reynolds numbers. Moreover, Fig. 15 reveals the dominance of the resolved stresses τ_{res} denoted by the dotted lines from the third lattice node and beyond toward the interior of the domain.

This is also the case when increasing the Reynolds number or the lattice spacing and thereby amplifying the wall function influences. The respective (large) predicted resolved shear stresses suddenly drop when entering the buffer layer in the direction of the wall. For the coarse grids, this decrease occurs almost abruptly. In conjunction with $\mathrm{Re}_\tau = 180$, the near-wall results of the coarse grid remain close to the finer grids because the mean velocity gradient is well captured. However, increasing the Reynolds numbers reveals larger disparities between resolved shear stress levels predicted by the coarse, medium, and fine grids near the wall. The latter is accompanied by a mismatch of the mean velocity gradient, which also induces an over-prediction of the turbulence energy production, cf. Fig. 16.

The SGS-contribution should balance the reduction of resolved turbulent shear when approaching the wall. However, if the wall-adjacent eddy viscosity and, thereby, the modeled shear stress are under-predicted, this is compensated by an over-predicted (mean) velocity gradient. In this regard, a poor resolution of the turbulence generating buffer layer poses a challenge to the present cumulant SGS/wall function combination, cf. the medium ($y_2^+ \approx 25$) and the coarse ($y_2^+ \approx 70$) grid results for $\mathrm{Re}_\tau = 550$, and all results for $\mathrm{Re}_\tau = 2000$ ($y_2^+ \approx \{60, \ldots, 250\}$). Since the wall function substantially attenuates the turbulent dynamics and does not recover abruptly on coarser meshes, this impedes the cumulant-based SGS model in a few wall-adjacent coarse grid nodes. Figure 17 displays the over-estimation of the mean velocity gradient near the wall in conjunction with the coarse grid simulations at $\mathrm{Re}_\tau = 550$ (red) and all simulations at $\mathrm{Re}_\tau = 2000$.

Likewise, Fig. 18 depicts the averaged normalized eddy viscosity $\bar{\nu}_t/\nu$ (left) and an estimate of the discrepancy between the predicted and the required eddy viscosity (right), which again outlines the near-wall defect for the higher Reynolds numbers.

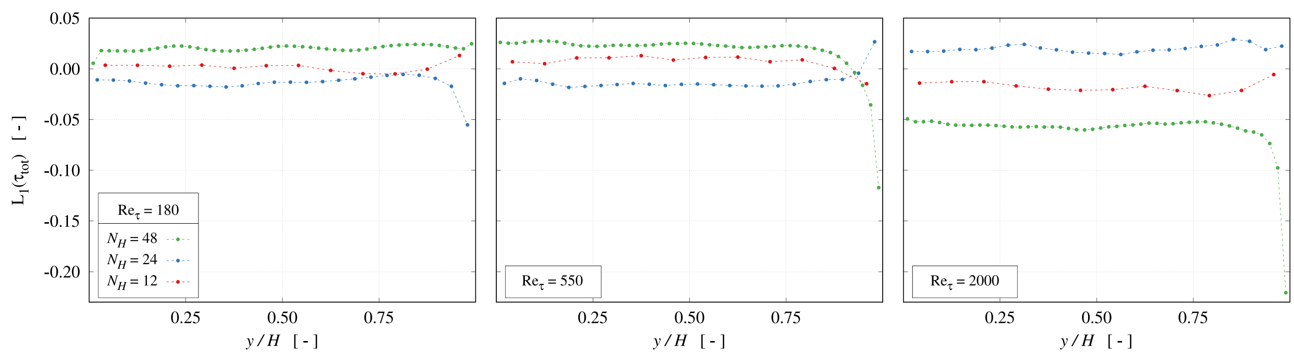

FIG. 14. Relative deviation of the non-dimensional total shear stress from a linear relation $L_1(\tau_{\mathrm{tot}}) = (\tau_{\mathrm{tot}} - \tau_{\mathrm{lin}})/\tau_{\mathrm{lin}}$, with $\tau_{\mathrm{lin}} = (1 - y/H)$.

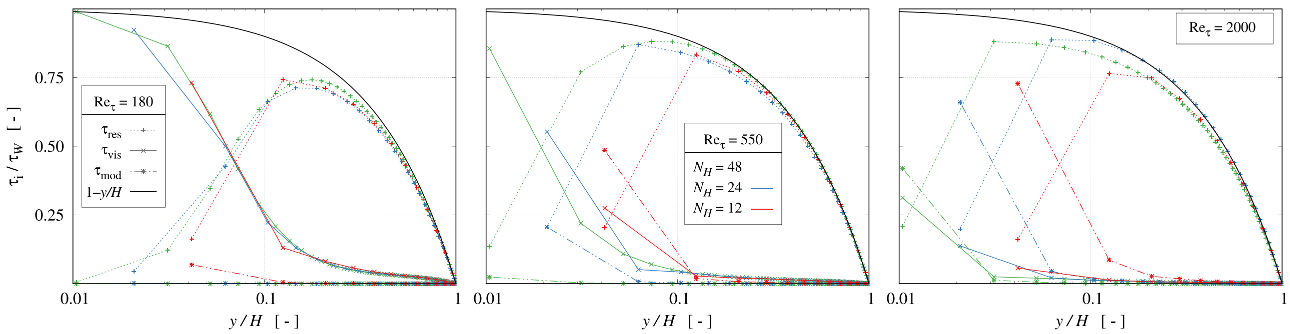

FIG. 15. Comparison of non-dimensional resolved (dotted), viscous (solid), and modeled (dashed) shear stress profiles with linear total stress relation $\tau_i/\tau_W = 1 - y/H$ (solid black line).

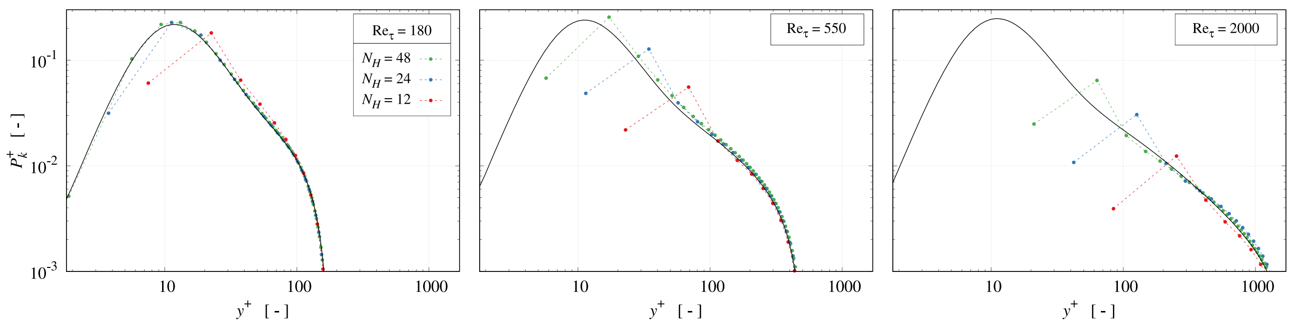

FIG. 16. Comparison of non-dimensional turbulence energy production rate $P_k^+ = -\overline{u'v'}\,\frac{\mathrm{d}\bar{u}}{\mathrm{d}y}\,[\cdot\frac{\nu}{u_\tau^4}]$ with DNS reference data.[83]

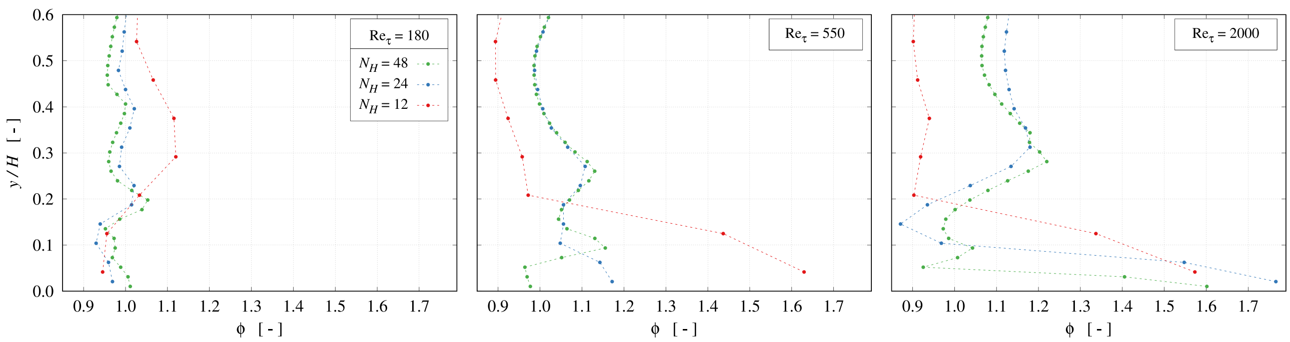

FIG. 17. Ratio of the predicted to the reconstructed velocity gradient $\phi = (\mathrm{d}\bar{u}/\mathrm{d}y)_{\mathrm{LBM}}/(\mathrm{d}\bar{u}/\mathrm{d}y)_{\mathrm{rec}}$ using second-order finite differences.

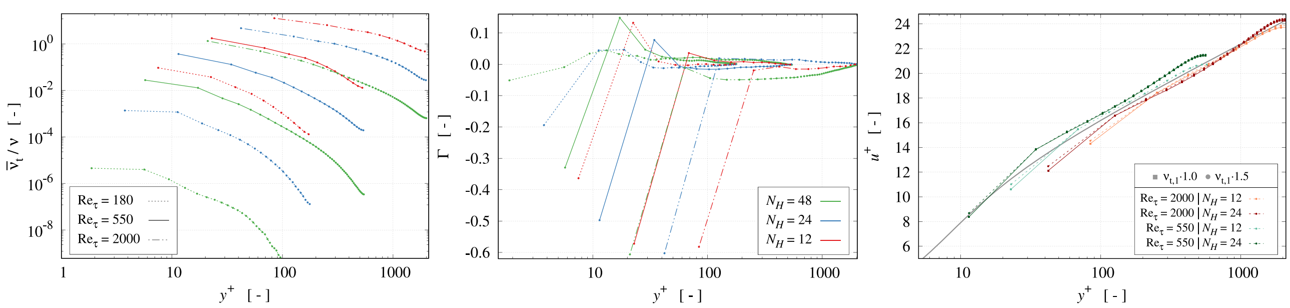

FIG. 18. Averaged non-dimensional eddy viscosity $\bar{\nu}_t/\nu$ (left), estimated discrepancy between the predicted and the required non-dimensional eddy viscosity (right) $\Gamma = [(\nu + \bar{\nu}_t)\,(\mathrm{d}\bar{u}/\mathrm{d}y)_{\mathrm{rec}} + |\overline{u'v'}|]/u_\tau^2 + y_{\mathrm{SI}}/H - 1$, and comparison of mean velocities in the buffer layer predicted with the present approach ($\nu_t \cdot 1.0$) and a 50% augmentation of the near-wall eddy-viscosity ($\nu_t \cdot 1.5$) against a second-order Spalding law[62] (gray line) (right).

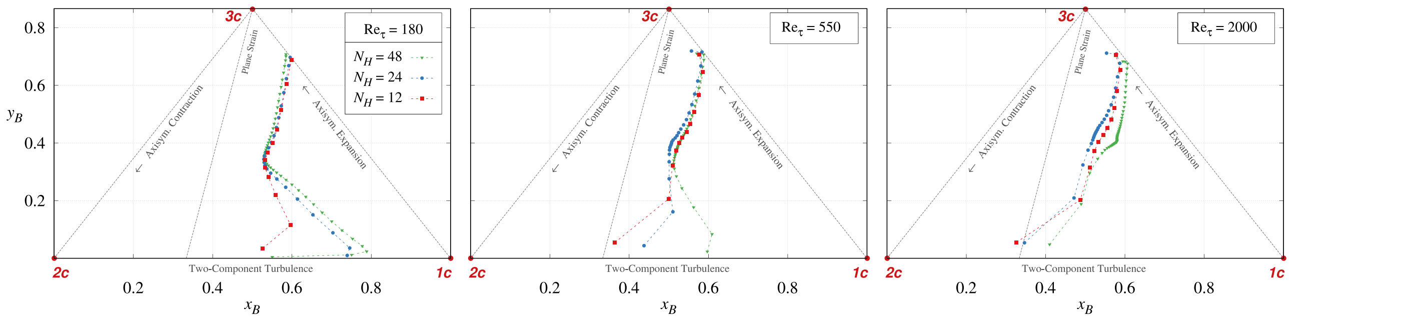

FIG. 19. Barycentric representation of the (resolved) Reynolds stress anisotropies. The abscissa ($y_B = 0$) refers to wall location.

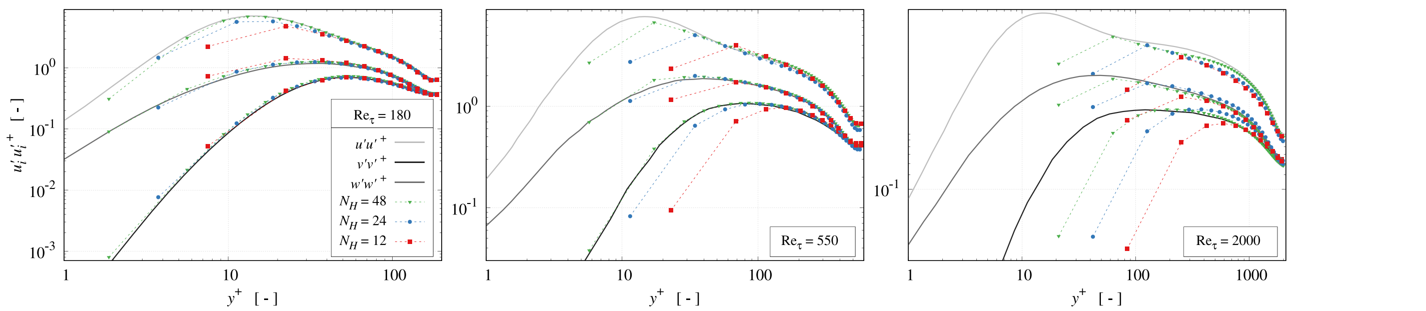

FIG. 20. Non-dimensional (resolved) Reynolds normal stresses supplemented by reference data.[60,61]

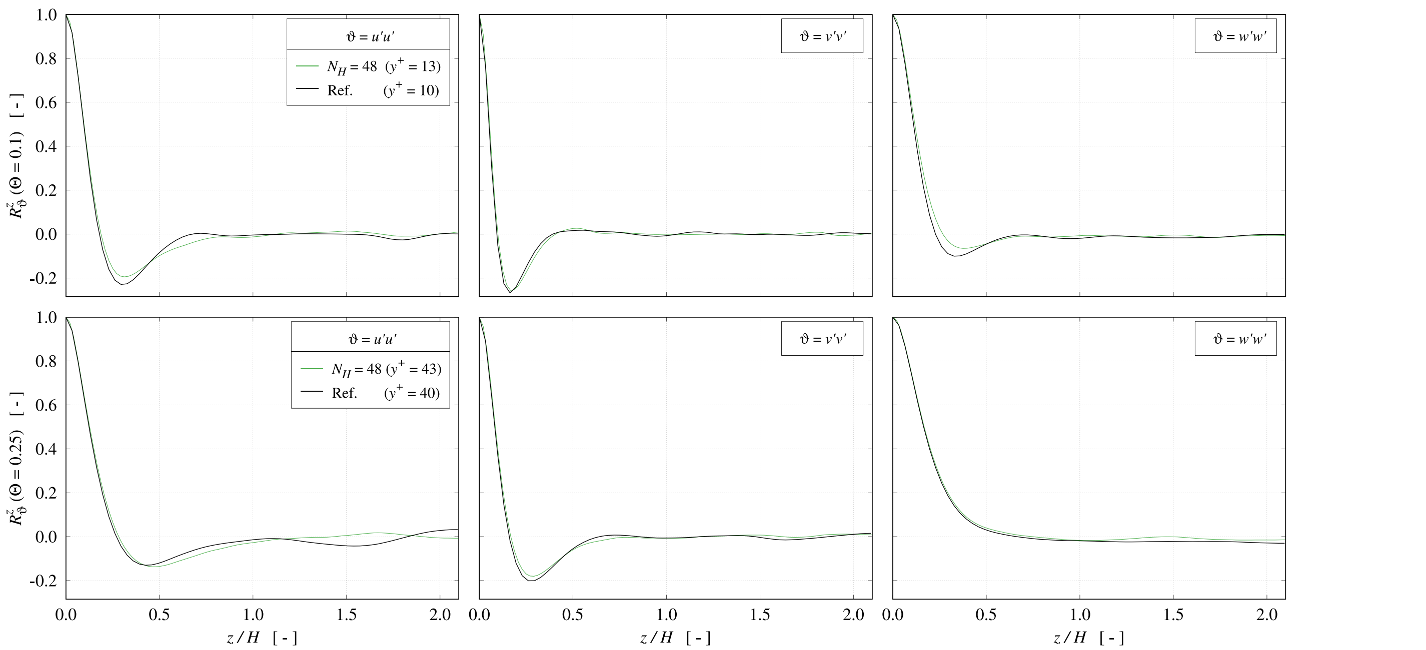

FIG. 21. Spanwise maxima-normalized two-point correlations obtained from the fine grid ($N_H = 48$) for $\mathrm{Re}_\tau = 180$ at $\Theta = 0.1$ (top) and $\Theta = 0.25$ (bottom) for $\vartheta = \{\overline{u'u'}, \overline{v'v'}, \overline{w'w'}\}$ (left, mid, and right). The pathlines are plotted in outer (z/H) scaling and compared to DNS reference data from Moser *et al.*[60] (solid black lines).

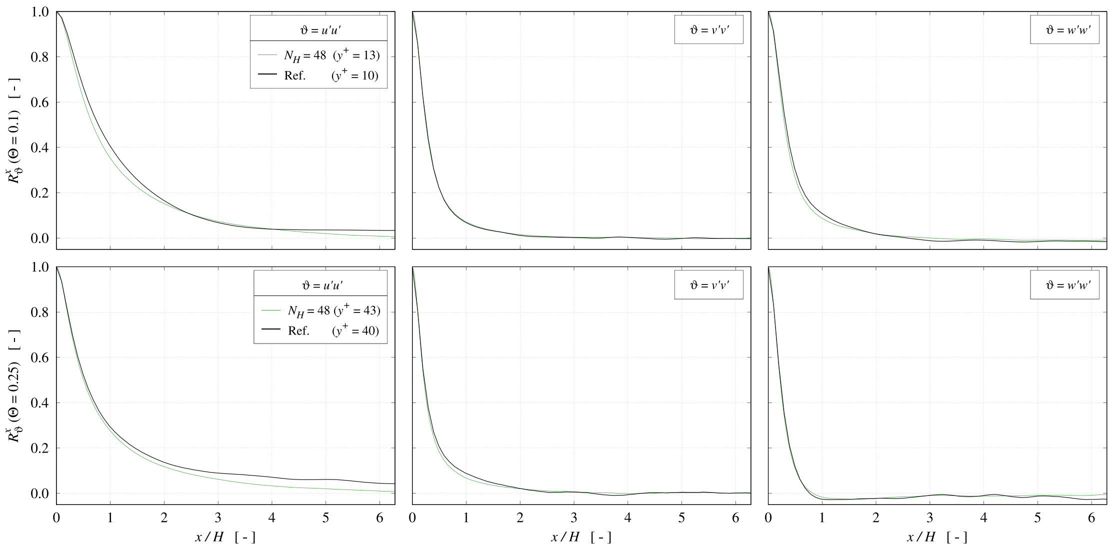

FIG. 22. Streamwise maxima-normalized two-point correlations obtained from the fine grid ($N_H = 48$) for $\mathrm{Re}_\tau = 180$ at $\Theta = 0.1$ (top) and $\Theta = 0.25$ (bottom) for $\vartheta = \{\overline{u'u'}, \overline{v'v'}, \overline{w'w'}\}$ (left, mid, and right). The pathlines are plotted in outer (x/H) scaling and compared to DNS reference data from Moser *et al.*[60] (solid black lines).

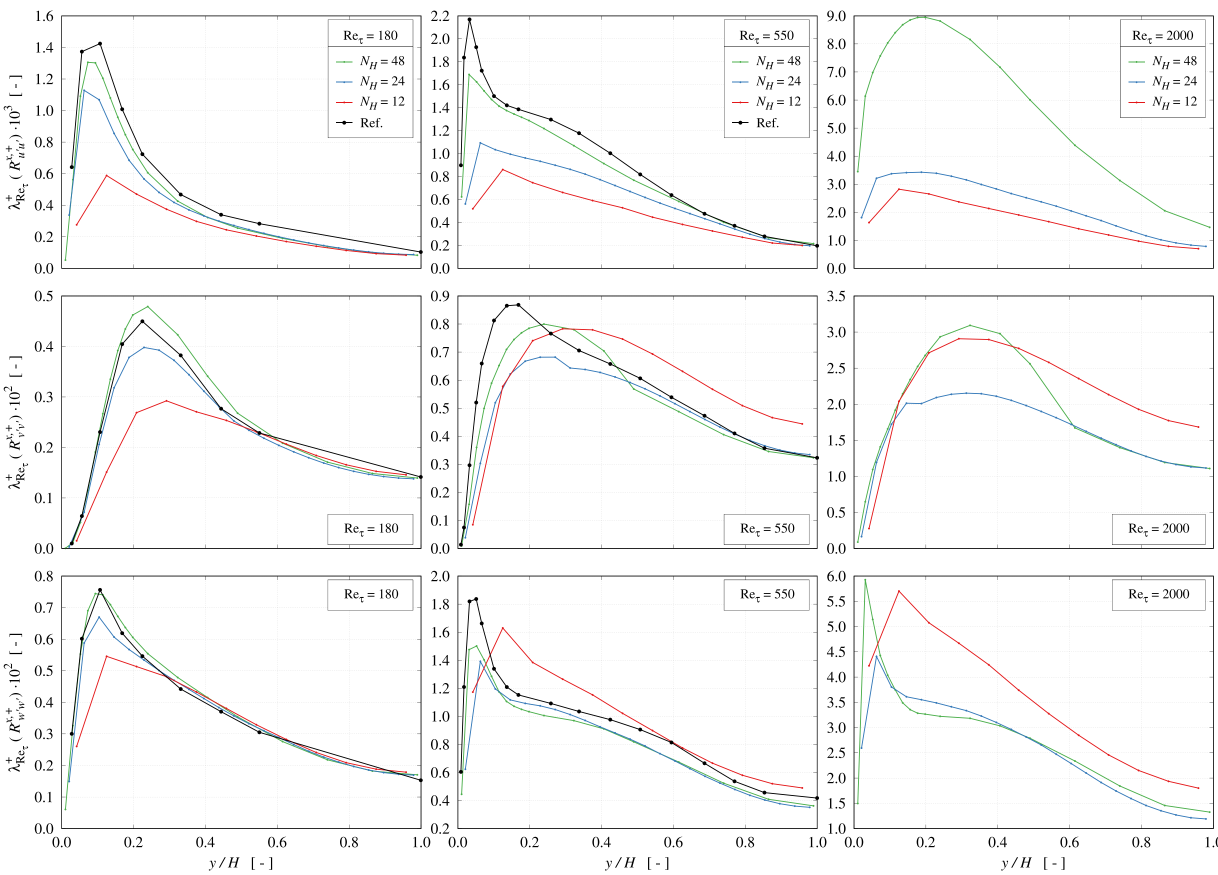

FIG. 23. Non-dimensional streamwise correlation lengths for $\overline{u'u'}$ (top), $\overline{v'v'}$ (mid), and $\overline{w'w'}$ (bottom) column-wise displayed for all three $\mathrm{Re}_\tau = \{180; 550; 2000\}$ (left, mid, and right) for each grid $N_H = \{12; 24; 48\}$ (red, blue, and green) plotted vs non-dimensional outer wall-normal coordinate. The abscissa range is scaled individually in each plot and row-wise constantly scaled by decimal power, i.e., 10^3 [$\overline{u'u'}$], respectively, 10^2 [$\overline{v'v'}$, $\overline{w'w'}$]. Reference data refer to $\mathrm{Re}_\tau = 180$ and $\mathrm{Re}_\tau = 590$, cf. Moser *et al.*[60]

While the eddy viscosity is generally negligible for $\mathrm{Re}_\tau = 180$ (dotted) and remains minor for $\mathrm{Re}_\tau = 550$ (solid), significant eddy viscosity levels are observed at $\mathrm{Re}_\tau = 2000$ (dashed), particularly for the coarse grid, where $\overline{\nu_t}/\nu \in [1; 10]$ over large portions of the domain. From Fig. 18(right), it is noted that the overshooting characteristics follow the soft transition displayed by empirical universal wall functions (e.g., according to Spalding[62]) and reduce when augmenting the eddy viscosity at the wall adjacent interior fluid nodes.

D. Resolved turbulence field

Figures 19 and 20 show the predicted resolved Reynolds stress anisotropies and profiles of the resolved normal stress components. Results of the present LBM are compared to DNS data (black lines) obtained from Moser *et al.*[60] and Bernardini *et al.*[61]

For the low Reynolds number $\mathrm{Re}_\tau = 180$, the SGS-contributions are negligible, cf. Fig. 18, and the resolved Reynolds stresses reveal a fair coincidence with the reference data. The anisotropy prediction deteriorates as the resolution coarsens, and the modeling influences increase. The respective left graphs of Figs. 19 and 20 clearly reveal an erroneous shift toward an isotropic distribution of the wall-parallel normal stresses $\overline{u'u'}$ and $\overline{w'w'}$ near the wall when the grid is coarsened.

Mind that the barycentric coordinate y_B vanishes at the wall, and the wall-normal velocity fluctuation v' is attenuated due to wall damping and wall function influences. As the Reynolds number increases, the resolution of the employed grids deteriorates, and the attenuation of the wall-normal fluctuation extends further toward the centerline. Simultaneously, the shift from 1c toward 2c-turbulence in the near-wall region proceeds.

Increasing the wall function influence by increasing the Reynolds number or reducing the resolution induces a strong reduction of the streamwise correlation length $\lambda^+(R^{x,+}_{u'u'})$, as outlined below. Moreover, the two-point correlations indicate that the under-resolved near-wall flow shares some features with the core flow.

E. Two-point correlations and correlations lengths

The occurrence and location of minima displayed by the spanwise (z) two-point correlations R^z_ϑ allow to identify structures and estimates their size. Figure 21 depicts these correlations obtained for $\mathrm{Re}_\tau = 180$ in the $\Theta = 0.1$ and $\Theta = 0.25$ planes.

Predictive agreement between the fine grid LBM results and the reference DNS data of Moser *et al.*[60] is generally fair. Streamwise vortices are indicated by the minima of $R^z_{\overline{v'v'}}$ located between $z/H \approx 0.17$ ($z^+ \approx 30$) at $\Theta = 0.1$ and $z/H \approx 0.28$ ($z^+ \approx 50$) at $\Theta = 0.25$ and provide an impression about their diameter. Consistent with formerly reported results, the $R^z_{\overline{v'v'}}$ minimum is located closer to the wall than the minimum of $R^z_{\overline{u'u'}}$. The latter separates the high-speed fluid from the

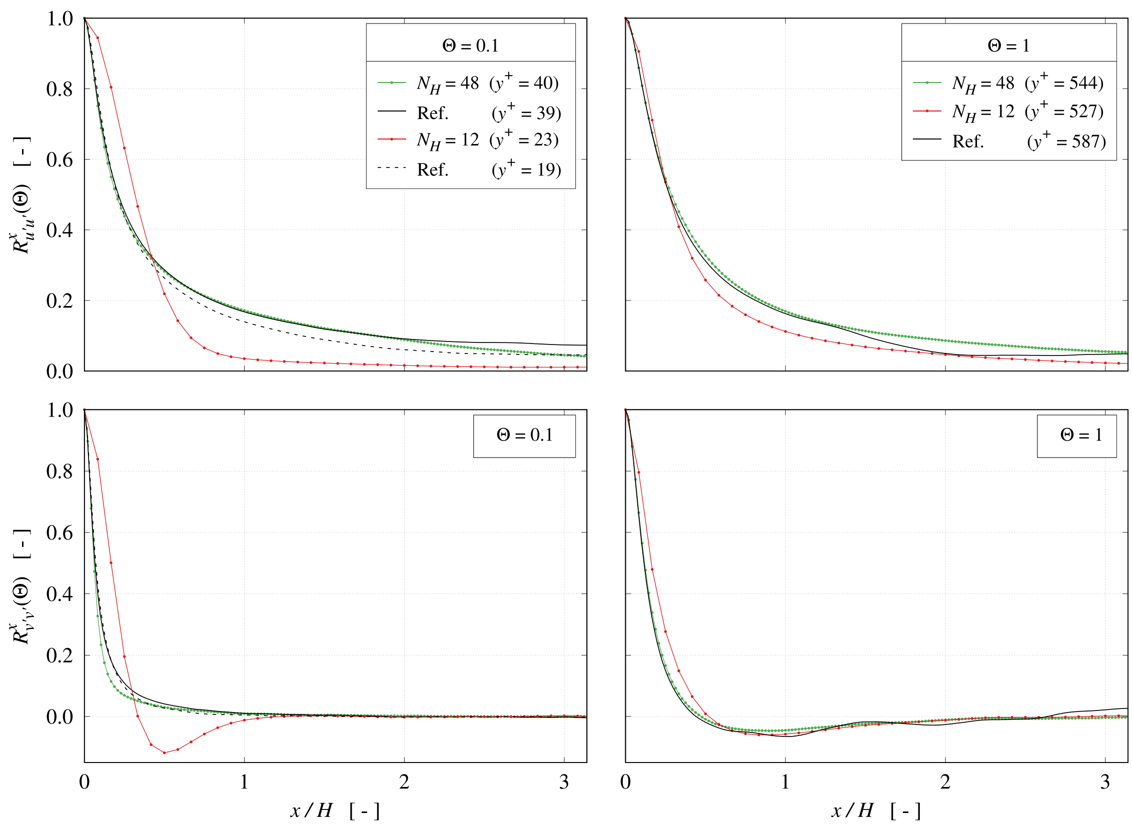

FIG. 24. Streamwise R^x_ϑ maxima-normalized $\vartheta = \overline{u'u'}$ (top) and $\vartheta = \overline{v'v'}$ (bottom) two-point correlations obtained from the fine ($N_H = 48$) and coarse ($N_H = 12$) for $\mathrm{Re}_\tau = 550$ at a near-wall [$\Theta = 0.1$, (left)] and the centerline position [$\Theta = 1$, (right)] supplemented by the reference data from Moser *et al.*[60] at $\mathrm{Re}_\tau = 590$.

low-speed fluid at approximately half the mean streak spacing. The evolution of the companion streamwise correlations is simpler and shows a fair predictive agreement, as indicated by the results in Fig. 22.

Identifying predictive differences from the various two-point correlations is sometimes intricate. Hence, integral values are frequently used to support an assessment. Former analysis, e.g., by Tritton,[85] reveals that the normalized streamwise correlation length of the streamwise velocity maximizes at the end of the buffer layer, e.g., around $y^+ = 20$–30, where the respective peak values significantly exceed the y^+-value and subsequently drop in the log-layer. Figure 23 describes the evolution of the predicted streamwise correlation lengths for all three normal stress components as a function of the Reynolds number and the grid resolution.

The LBM data are compared with reference data extracted from DNS simulations of Moser *et al.*[60] for $\mathrm{Re}_\tau = \{180, 590\}$ since no other data are available for the large Reynolds number. As mentioned above, the figures prove a significant length-scale reduction in the streamwise direction for the coarse grids. The latter yields similarities between the near-wall and the centerline regions of the respective two-point correlations, as displayed in Fig. 24.

On the contrary, the spanwise length scales depicted by Fig. 25 are generally much smaller and also reflect smaller gradients in the vertical direction. Hence, grid resolution influences are far less pronounced than in the streamwise direction.

F. Energy spectra

Figures 26 and 27 compare the computed streamwise and spanwise energy spectra for all Reynolds numbers with reference data obtained from DNS simulations of Moser *et al.*[60] for $\mathrm{Re}_\tau = \{180; 590\}$ and Lee and Moser.[83] for $\mathrm{Re}_\tau = 2000$.

Displayed results refer to four different wall distances, i.e., $y/H = \Theta = \{0.1, 0.25, 0.5, 1\}$, and are restricted to fine grid LBM computations with $N_H = 48$ points across the half-height H, since the present resolution *automatically* deteriorates when the Reynolds number is increased.

With regard to $\mathrm{Re}_\tau = 180$, the LBM results show convincing agreement with the reference DNS data, with minor reservations for the wall nearest location where the y^+-values differ. This case is certainly less challenging, as the resolution is close to DNS.

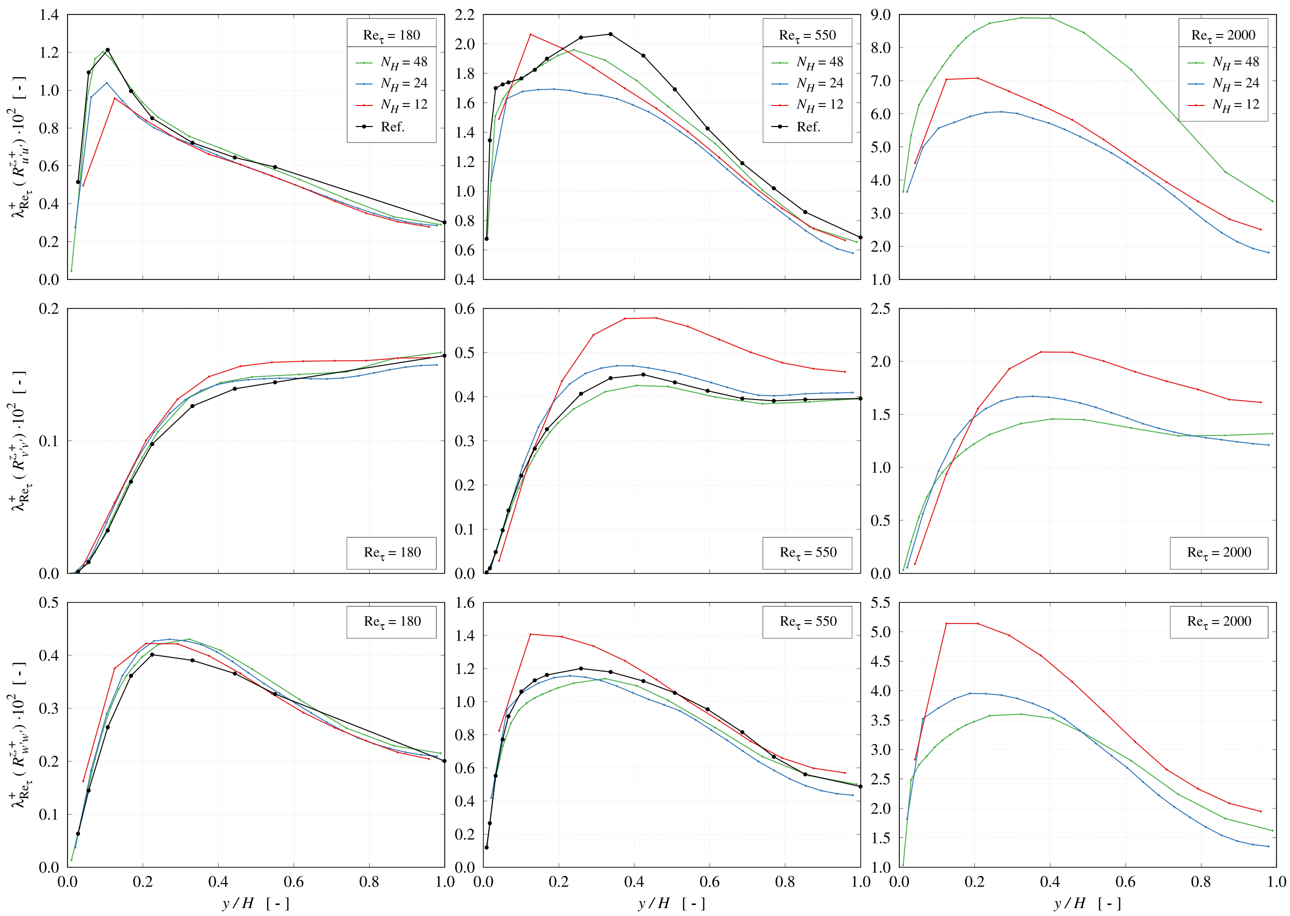

FIG. 25. Non-dimensional spanwise correlation lengths for $\overline{u'u'}$ (top), $\overline{v'v'}$ (mid), and $\overline{w'w'}$ (bottom) column-wise displayed for all three $\mathrm{Re}_\tau = \{180; 550; 2000\}$ (left, mid, and right) and each grid $N_H = \{12; 24; 48\}$ (red, blue, and green). Reference data refer to $\mathrm{Re}_\tau = 180$ and $\mathrm{Re}_\tau = 590$ extracted from Moser *et al.*[60]

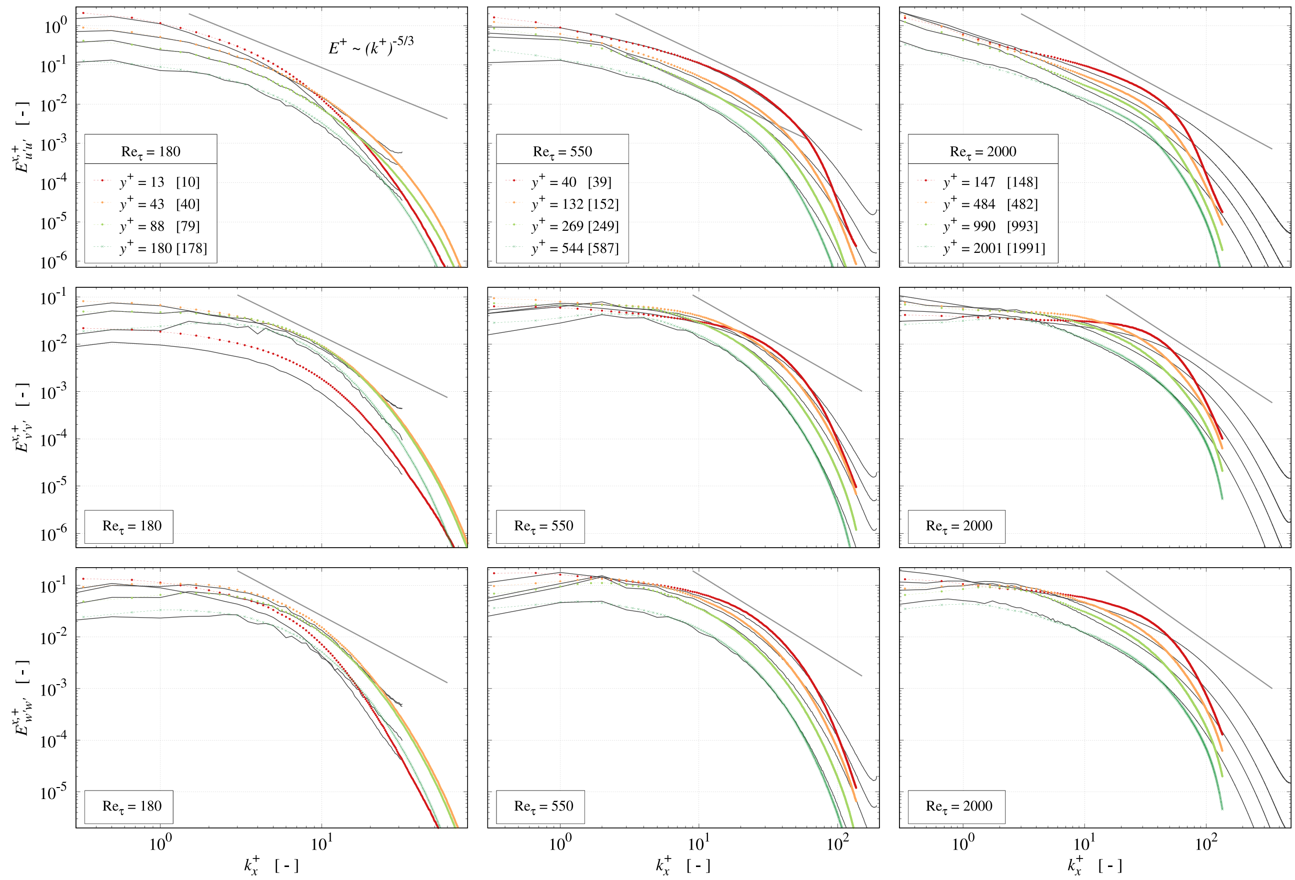

FIG. 26. Streamwise turbulent energy spectra for $\vartheta = \{\overline{u'u'}, \overline{v'v'}, \overline{w'w'}\}$ (top, mid, and bottom) obtained from fine grid ($N_H = 48$) simulations for all three $Re_\tau = \{180; 550; 2000\}$ (left, mid, and right) at varying wall-normal positions $\Theta = \{0.1; 0.25; 0.5; 1\}$ (dark red, orange, light green, and dark green). Solid lines display reference data of Moser *et al.*[60] for $Re_\tau = \{180; 590\}$ and Lee and Moser.[83] for $Re_\tau = 2000$. Data are labeled by the $y^+ = y^+(\Theta, N_H = 48, Re_\tau)$ values, cf. Table III, and complemented by the closest values of the reference dataset as indicated in square brackets. Constant *y*-intercepts apply row-wise (ϑ), and *x*-ranges coincide column-wise (Re_τ). Additionally, the $E^+ \sim (k^+)^{-5/3}$ proportionality of the inertial range is displayed.

With attention directed to $Re_\tau = 550$, the resolution refers to $\Delta x^+ = 11.5$, and the influence of the resolution-triggered regularization is clearly observed in the evolution of the streamwise spectra. As already discussed for more complex periodic hill flows in Gehrke and Rung,[26] the steep decline of the higher wave number parts of the spectra ($k_x^+ > 60$) is induced by the regularization and helps to suppress potential instabilities. Except for the dissipative high wave number regime and a slight tendency to pull some of the unresolved high-wave number content into the upper-wave numbers of the inertial subrange for $\Theta = 0.1$ (red) and $\Theta = 0.25$ (orange), predictive agreement with the reference DNS data is deemed fair. Results displayed for $Re_\tau = 2000$ were compiled for $\Delta x^+ = 42$ and reveal both regularization and SGS influences. Results for the dominating $E^{x,+}_{u'u'}$ spectra are in fair agreement with the references data in the energy-containing range. The width of the inertial subrange is substantially reduced, and the LBM spectra start declining with an increasing slope at $k_x^+ > 40[60]$ for the lower (upper) locations. The increase in the inertial subrange content is more pronounced for the lower locations (red and orange) and affects the spectra at $\Theta = 0.5$ (light green). Mind that the result obtained for the spanwise spectra depicted in Fig. 27 generally agrees better with the reference data for the higher Reynolds numbers, as could be expected from the two-point correlations and the correlation lengths discussed above.

Figure 28 compares the stream- and spanwise energy spectra for $Re_\tau = 2000$ obtained on the coarse and the fine grid for the $\overline{u'u'}$ and $\overline{w'w'}$ components, respectively. The figure confirms the previous discussion.

Grid coarsening reduces the resolved part of the inertial subrange to $k_x^+ \lesssim 20$ and introduces an earlier onset of dissipation. Nonetheless, the low frequency dynamics is still captured as also outlined by Fig. 29.

G. Application to higher Reynolds number and comparison to conventional SGS

To convey the capabilities of the present suggestion, we supplement results for a Reynolds number of $Re_\tau = 5200$ against DNS data published by Lee and Moser.[83] Figure 30 displays the predictions of the mean flow, shear stress contributions, and Reynolds normal

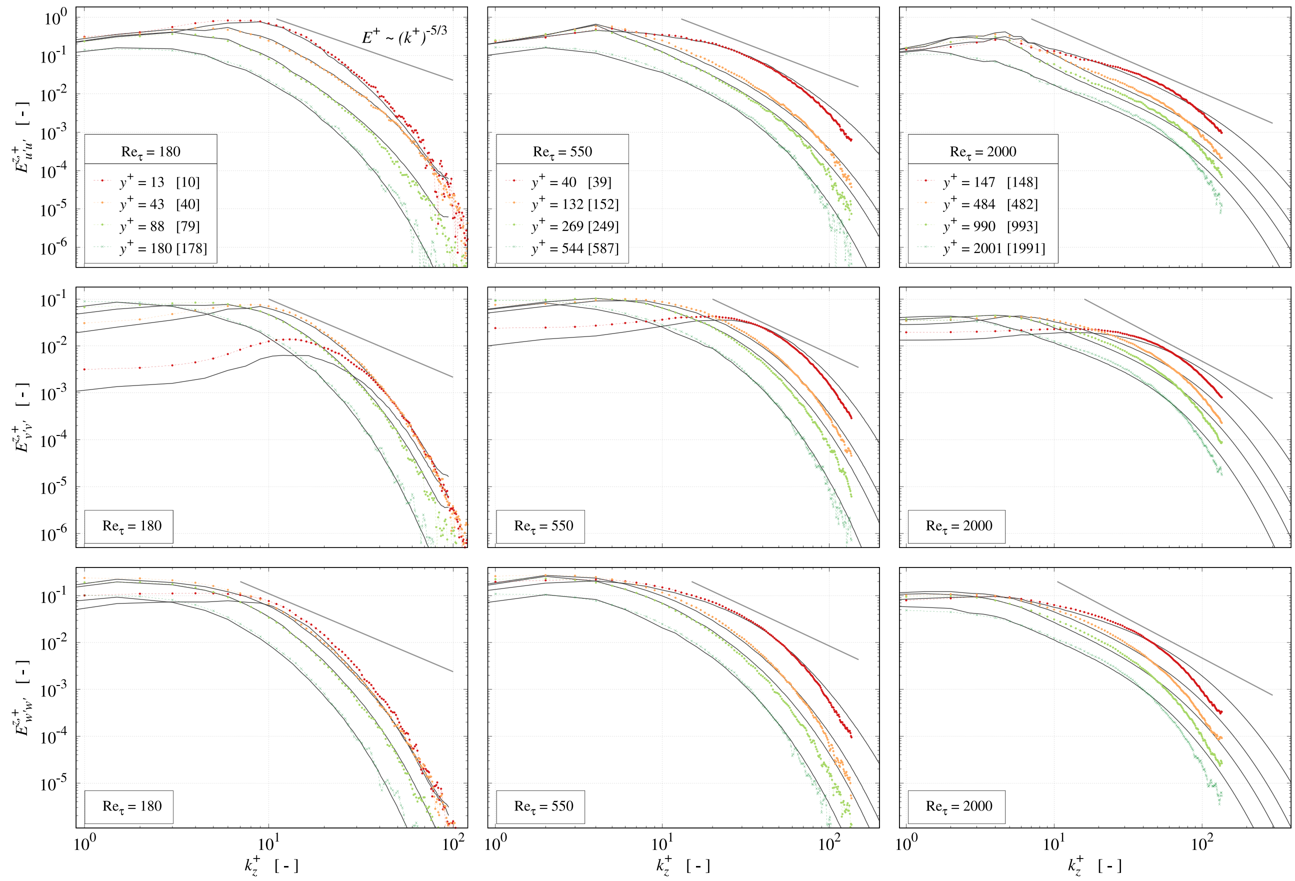

FIG. 27. Spanwise turbulent energy spectra for $\vartheta = \{\overline{u'u'}, \overline{v'v'}, \overline{w'w'}\}$ (top, mid, and bottom) obtained from the fine grid ($N_H = 48$) simulations for all three $\mathrm{Re}_\tau = \{180; 550; 2000\}$ (left, mid, and right) at varying wall-normal positions $\Theta = \{0.1; 0.25; 0.5; 1\}$ (dark red, orange, light green, and dark green). Solid lines display reference data of Moser *et al.*[60] for $\mathrm{Re}_\tau = \{180; 590\}$ and Lee and Moser.[83] for $\mathrm{Re}_\tau = 2000$. Data are labeled by the $y^+ = y^+(\Theta, N_H = 48, \mathrm{Re}_\tau)$ values, cf. Table III, and complemented by the closest values of the reference dataset as indicated in square brackets. Constant *y*-intercepts apply row-wise (ϑ), and *x*-ranges coincide column-wise (Re_τ). Additionally, the $E^+ \sim (k^+)^{-5/3}$ proportionality of the inertial range is displayed.

stresses. The employed wall function refers to $u^+(y^+) = \log(y^+)/0.39 + 4.7$ which is in line with the Lee and Moser.[83]

Due to the enhanced distance of the first fluid node, buffer zone and transition influences diminish, and predictive agreement with DNS data slightly improves in comparison with $\mathrm{Re}_\tau = 2000$.

Appendix C outlines a comparison of mean velocities and resolved Reynolds stresses against conventional LES approaches using $\mathscr{C}_S = 0.15$ in line with Pope,[86] which is often used in industrial applications. The comparison refers to $\mathrm{Re}_\tau = \{180, 550, 2000\}$ and reveals the benefits of the present approach, in particular an improved level of resolved stresses. The overshoot phenomenon is also observed for $\mathrm{Re}_\tau = 2000$ with the conventional approach, but related near wall predictions clearly deteriorate for lower Reynolds numbers and improved resolutions.

VI. CONCLUSION

This paper addresses the predictive performance of the LB method based upon a modified cumulant collision operator. Attention is restricted to turbulent channel flows, regarded as building blocks for modeling engineering shear flows. Investigations originate from low Reynolds numbers ($\mathrm{Re}_\tau = 180$) and DNS-type resolutions with $\Delta x^+ < 4$ and extent to computationally more demanding Reynolds numbers ($\mathrm{Re}_\tau = 5200$) and coarse grid resolutions featuring $\Delta x^+ > 400$, using isotropic homogeneous Cartesian grids.

Previous investigations demonstrated the remarkable turbulence prediction capabilities of the cumulant LBM. Except for the general regularization, no dedicated turbulence model is needed in well-resolved flows featuring $\Delta x^+ \lesssim 10$. However, literature reported results also reveal the limitations of the regularized cumulant LBM for coarse resolutions, which quickly occur at higher Reynolds numbers. The present work aims to advance these limits using two simple modifications of the baseline model. First, an alternative regularization is suggested, which is deemed sufficient to dissipate the kinetic energy of the large wave numbers and accurately compute flows with fine to moderate resolutions characterized by $\Delta x^+ \lesssim 20$. Second, a third-order cumulant expression is employed to formulate a dynamic Smagorinsky-type SGS model that acts on smaller wave numbers. Both modifications employ the resolution through the cell Reynolds

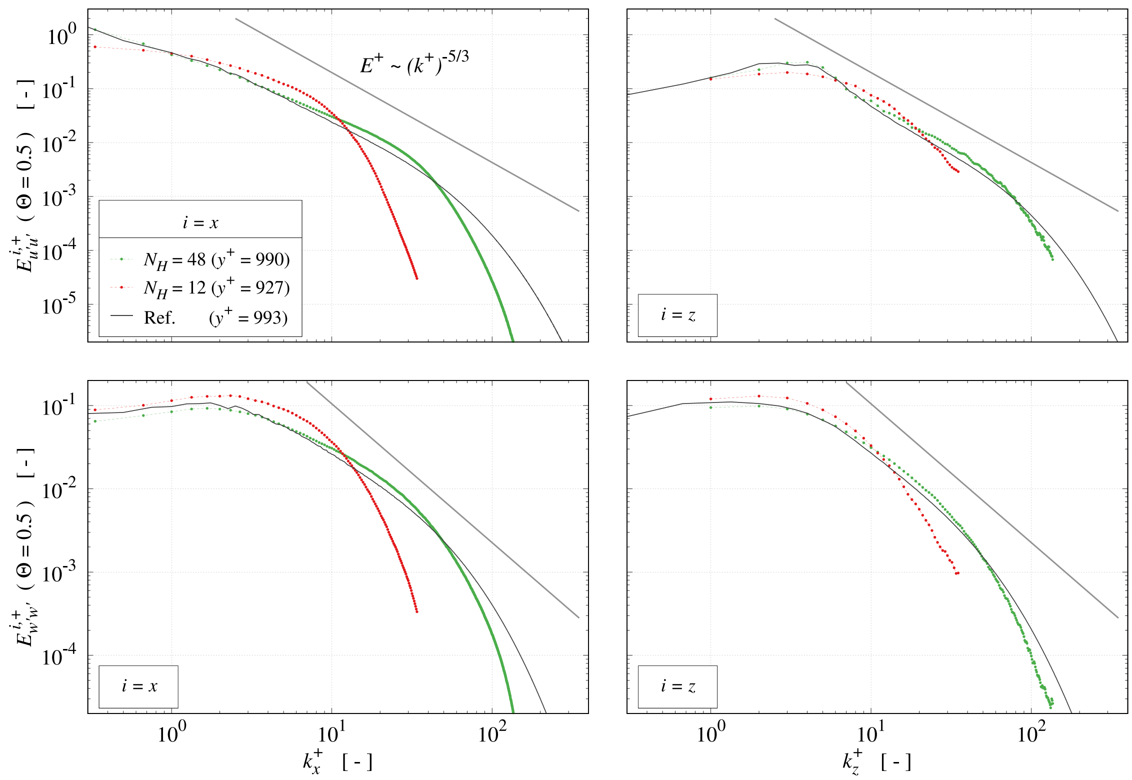

FIG. 28. Stream- (left) and spanwise (right) turbulent energy spectra for $\vartheta = \{\overline{u'u'}, \overline{w'w'}\}$ (top and bottom) obtained from fine (green) and coarse (red) grid simulations for $Re_\tau = 2000$ at $\Theta = 0.5$. Solid lines display reference data of Lee and Moser.[83] The correlating N_H-dependent y^+-values of $\Theta = 0.5$ are given in the upper left key.

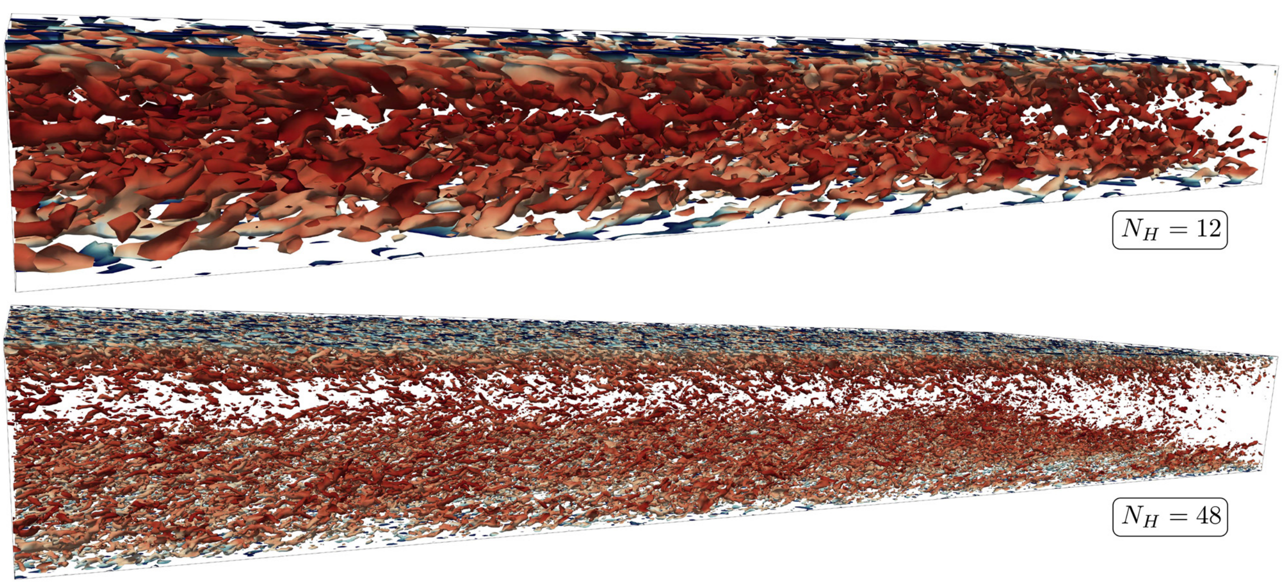

FIG. 29. Illustration of turbulent structures based on the non-dimensional streamwise vorticity component $\omega_x^+ = (\mathrm{d}v/\mathrm{d}z - \mathrm{d}w/\mathrm{d}y)\, N_H/u_\tau$ for $Re_\tau = 2000$ obtained from the coarse (top) and fine (bottom) grids. Displayed isosurfaces refer to $0.2\omega^+_{x,\max}$ and are colored by the velocity magnitude.

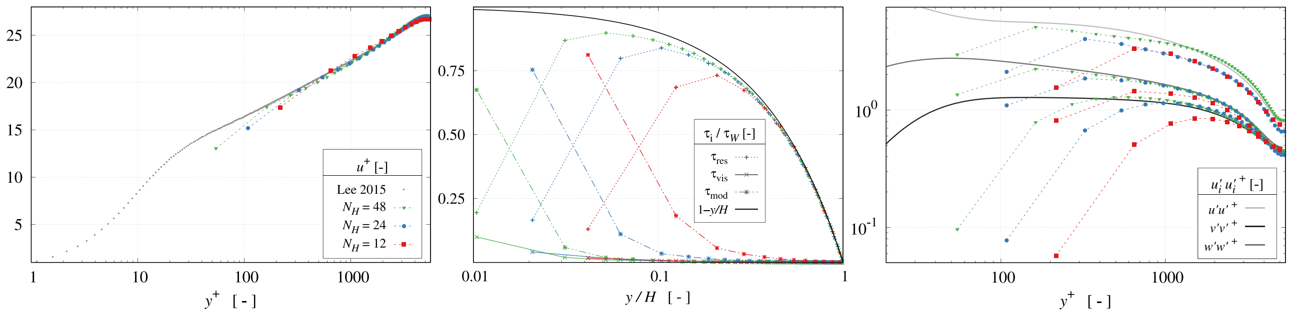

FIG. 30. Non-dimensional mean velocity profiles (left), shear stress contributions (center), and normalized (resolved) Reynolds normal stresses (right) for $Re_\tau = 5200$. Displayed reference data for u^+ and $\overline{u_i' u_i'}^+$ refer to DNS data published by Lee and Moser.[83]

number (spatial) and the Mach number (temporal). They seamlessly vanish in the fine-grid limit and interact favorably with the investigated cases. Furthermore, coupling to a wall function involves minimal additional efforts and supports the transition to the fine-grid limit.

Results indicate a remarkable robustness and predictive performance of the modified cumulant model. A remaining deficit refers to the interaction between the SGS model and the wall function, e.g., $\Delta x^+ \gtrsim 35$, where the dynamic character of the SGS suffers from the missing dynamics of the wall function in coarse resolutions. In conclusion, the very near-wall eddy viscosity is predicted to be too small, which induces an overshoot of the predicted velocity gradient between the two wall-nearest lattices to balance the resolved shear in the interior. However, this does not significantly harm the remainder of the flow, and the prediction of the turbulent dynamics rapidly recovers toward the interior flow, which is also supported by very large Reynolds number studies.

The deficit could be addressed by augmenting the wall function and adding a related eddy viscosity contribution in the transition, i.e., the buffer-layer regime. More severe open issues refer to the geometric generalization of the wall function and an assessment or rather adaptation of the suggested modifications for anisotropic grids, which will be the subject of future studies.

ACKNOWLEDGMENTS

The authors thank H. Asmuth (Uppsala University, Sweden) for substantial support and valuable discussions regarding his wall function approach.

Publishing fees supported by Funding Programme *Open Access Publishing* of Hamburg University of Technology (TUHH).

AUTHOR DECLARATIONS

Conflict of Interest

The authors have no conflicts to disclose.

Author Contributions

Martin Gehrke: Conceptualization (equal); Investigation (lead); Methodology (equal); Software (lead); Validation (lead); Visualization (lead); Writing – original draft (equal); Writing – review and editing (equal). **Thomas Rung:** Conceptualization (equal); Methodology (equal); Supervision (lead); Writing – original draft (equal); Writing – review and editing (equal).

DATA AVAILABILITY

The data that support the findings of this study are available from the corresponding author upon reasonable request.

APPENDIX A: WALL FUNCTION POLYNOMIALS

The C^1-polynomials $u^+_{Re_\tau}(y^+)$, cf. Fig. 31, deposited in the wall function approach, cf. Sec. II D, are given by (rounded to two decimal places)

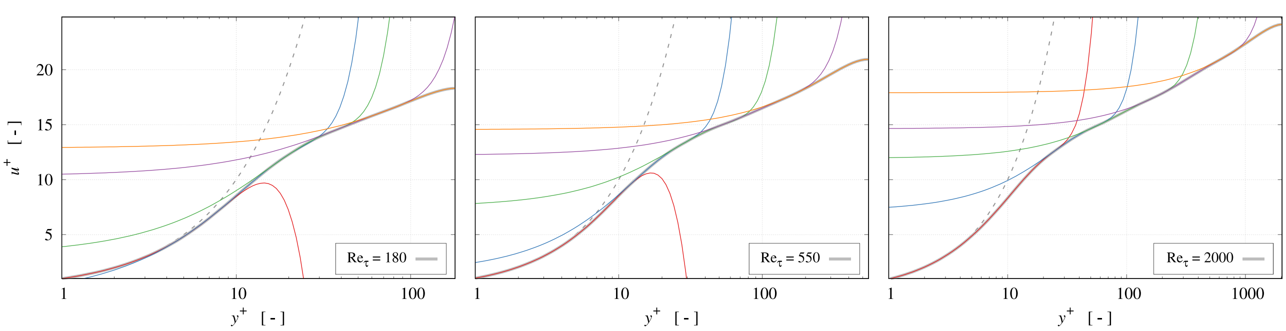

FIG. 31. Polynomial $u^+(y^+)$ reconstruction of the reference data[61,82] for the three underlying Reynolds numbers $Re_\tau = \{180; 550; 2000\}$.

$$u^+_{180}(y^+) = \begin{cases} -1.69\times10^{-03}(y^+)^3 + 1.95\times10^{-03}(y^+)^2 + 9.96\times10^{-01}y^+ + 7.68\times10^{-04}, & y^+ < 7,\\ +5.57\times10^{-04}(y^+)^3 - 4.38\times10^{-02}(y^+)^2 + 1.30\times10^{0}\ y^+ - 6.58\times10^{-01}, & 7 \le y^+ < 20,\\ +1.47\times10^{-04}(y^+)^3 - 1.72\times10^{-02}(y^+)^2 + 7.40\times10^{-01}y^+ + 3.17\times10^{0}, & 20 \le y^+ < 40,\\ +5.95\times10^{-06}(y^+)^3 - 1.51\times10^{-03}(y^+)^2 + 1.60\times10^{-01}y^+ + 1.03\times10^{+01}, & 40 \le y^+ < 80,\\ -4.89\times10^{-08}(y^+)^3 - 1.43\times10^{-04}(y^+)^2 + 5.75\times10^{-02}y^+ + 1.29\times10^{+01}, & 80 \le y^+ < 180, \end{cases} \tag{A1}$$

$$u^+_{550}(y^+) = \begin{cases} -7.03\times10^{-04}(y^+)^3 - 1.40\times10^{-02}(y^+)^2 + 1.07\times10^{0}\ y^+ - 1.77\times10^{-02}, & y^+ < 12,\\ +2.93\times10^{-04}(y^+)^3 - 2.73\times10^{-02}(y^+)^2 + 9.54\times10^{-01}y^+ + 1.53\times10^{0}, & 12 \le y^+ < 28,\\ +2.52\times10^{-05}(y^+)^3 - 4.60\times10^{-03}(y^+)^2 + 3.14\times10^{-01}y^+ + 7.52\times10^{0}, & 28 \le y^+ < 53,\\ +5.75\times10^{-07}(y^+)^3 - 2.94\times10^{-04}(y^+)^2 + 6.64\times10^{-02}y^+ + 1.22\times10^{+01}, & 53 \le y^+ < 143,\\ -3.15\times10^{-09}(y^+)^3 - 1.81\times10^{-05}(y^+)^2 + 2.25\times10^{-02}y^+ + 1.46\times10^{+01}, & 143 \le y^+ < 550, \end{cases} \tag{A2}$$

$$u^+_{2000}(y^+) = \begin{cases} +5.12\times10^{-04}\ (y^+)^3 - 4.06\times10^{-02}(y^+)^2 + 1.21\times10^{0}\ y^+ - 2.15\times10^{-01}, & y^+ < 24,\\ +2.63\times10^{-05}\ (y^+)^3 - 4.73\times10^{-03}(y^+)^2 + 3.20\times10^{-01}y^+ + 7.17\times10^{0}, & 24 \le y^+ < 60,\\ +5.10\times10^{-07}\ (y^+)^3 - 2.91\times10^{-04}(y^+)^2 + 6.73\times10^{-02}y^+ + 1.19\times10^{+01}, & 60 \le y^+ < 182,\\ +1.03\times10^{-08}\ (y^+)^3 - 2.25\times10^{-05}(y^+)^2 + 2.02\times10^{-02}y^+ + 1.46\times10^{+01}, & 182 \le y^+ < 623,\\ -8.79\times10^{-11}(y^+)^3 - 1.10\times10^{-06}(y^+)^2 + 5.66\times10^{-03}y^+ + 1.79\times10^{+01}, & 623 \le y^+ < 2000, \end{cases} \tag{A3}$$

APPENDIX B: EXPLICIT IMPLEMENTATION OF THE APPLIED CUMULANT COLLISION OPERATOR

The present explicit depiction of the collision operator in cumulant space is valid for specific choice of relaxation rates as particularly outlined in Sec. II B. Subsequently, $\rho = 1 + \delta\rho$ is the density and $\boldsymbol{u} = (u, v, w)^\top$ denotes the velocity vector. The underlying implementation rests on the well-conditioned computation of $\delta\rho$ and $\boldsymbol{u}$. Their explicit listing is left out here, and the reader is referred to either Geier *et al.*,[22] Appendix J, or Gehrke and Rung,[26] Appendix B for a thorough review.

Initially, the zeroth and first-order cumulants are related to macroscopic flow quantities and are, thus, conserved properties during collision. This implies omitting their relaxation, whereby

$$C^*_{000} = C_{000}, \tag{B1}$$

$$C^*_{100} = C_{100},\ C^*_{010} = C_{010},\ C^*_{001} = C_{001} \tag{B2}$$

holds. The second-order cumulants' collision reads

$$C^*_{110} = (1-\omega_1)\,C_{110}, \tag{B3}$$

$$C^*_{101} = (1-\omega_1)\,C_{101}, \tag{B4}$$

$$C^*_{011} = (1-\omega_1)\,C_{011}, \tag{B5}$$

and

$$C^*_{200} = \big[(1-\omega_1)(2C_{200} - C_{020} - C_{002}) - a_1 - a_2 + a_3\big]/3, \tag{B6}$$

$$C^*_{020} = \big[(1-\omega_1)(2C_{020} - C_{200} - C_{002}) + 2a_1 - a_2 + a_3\big]/3, \tag{B7}$$

$$C^*_{002} = \big[(1-\omega_1)(2C_{002} - C_{200} - C_{020}) - a_1 + 2a_2 + a_3\big]/3 \tag{B8}$$

featuring the following variables:

$$a_1 = 3\,\rho\,(1-\omega_1/2)\,(u^2\,D_x\,u - v^2\,D_y\ v), \tag{B9}$$

$$a_2 = 3\,\rho\,(1-\omega_1/2)\,(u^2\,D_x\,u - w^2\,D_z\,w), \tag{B10}$$

$$a_3 = \delta\rho - 3\,\rho\,(1-1/2)\,(u^2\,D_x\,u + v^2\,D_y\,v + w^2\,D_z\,w). \tag{B11}$$

These contain first-order derivatives of the macroscopic velocity vector

$$D_x\,u = \omega_1/(2\,\rho)\,(-2\,C_{200} + C_{020} + C_{002}) - 1/(2\,\rho)\,(C_{200} + C_{020} + C_{002} - \delta\rho), \tag{B12}$$

$$D_y\,v = \omega_1/(2\,\rho)\,(C_{200} + 2\,C_{020} + C_{002}) - 1/(2\,\rho)\,(C_{200} + C_{020} + C_{002} - \delta\rho), \tag{B13}$$

$$D_z\,w = \omega_1/(2\,\rho)\,(C_{200} + C_{020} + 2\,C_{002}) - 1/(2\,\rho)\,(C_{200} + C_{020} + C_{002} - \delta\rho). \tag{B14}$$

The third-order collision step reads

$$C^*_{102} = \Big[(1-\omega^{\mathscr{C}}_{3,1})(C_{120}+C_{102}) - (1-\omega^{\mathscr{C}}_{4,2})(C_{120}-C_{102})\Big]/2, \tag{B15}$$

$$C^*_{120} = \Big[(1-\omega^{\mathscr{C}}_{3,1})(C_{120}+C_{102}) + (1-\omega^{\mathscr{C}}_{4,1})(C_{120}-C_{102})\Big]/2, \tag{B16}$$

$$C^*_{012} = \Big[(1-\omega^{\mathscr{C}}_{3,2})(C_{210}+C_{012}) - (1-\omega^{\mathscr{C}}_{4,2})(C_{210}-C_{012})\Big]/2, \tag{B17}$$

$$C^*_{210} = \Big[(1-\omega^{\mathscr{C}}_{3,2})(C_{210}+C_{012}) + (1-\omega^{\mathscr{C}}_{4,2})(C_{210}-C_{012})\Big]/2, \tag{B18}$$

$$C^*_{021} = \Big[(1-\omega^{\mathscr{C}}_{3,3})(C_{201}+C_{021}) - (1-\omega^{\mathscr{C}}_{4,3})(C_{201}-C_{021})\Big]/2, \tag{B19}$$

$$C^*_{201} = \Big[(1-\omega^{\mathscr{C}}_{3,3})(C_{201}+C_{021}) + (1-\omega^{\mathscr{C}}_{4,3})(C_{201}-C_{021})\Big]/2, \tag{B20}$$

and

$$C^*_{111} = (1-\omega^{\mathscr{C}}_5)\,C_{111}, \tag{B21}$$

where the regularized relaxation rates, cf. Sec. II B 1 [Eqs. (16)–(22)hx2013;(22)], occur. Fourth-order relaxation includes

$$C^*_{220} = \big[2\,a_4\,(D_x\,u - 2\,D_y\,v + D_z\,w) + 2\,a_4\,(D_x\,u + D_y\,v - 2\,D_z\,w) - 4\,a_4\,(D_x\,u + D_y\,v + D_z\,w)\big]/9, \quad \text{(B22)}$$

$$C^*_{022} = \big[-2\,a_4\,(D_x\,u + D_y\,v - 2\,D_z\,w) - 4\,a_4\,(D_x\,u + D_y\,v + D_z\,w)\big]/9, \quad \text{(B23)}$$

$$C^*_{202} = \big[-2\,a_4\,(D_x\,u - 2\,D_y\,v + D_z\,w) - 4\,a_4\,(D_x\,u + D_y\,v + D_z\,w)\big]/9 \quad \text{(B24)}$$

with

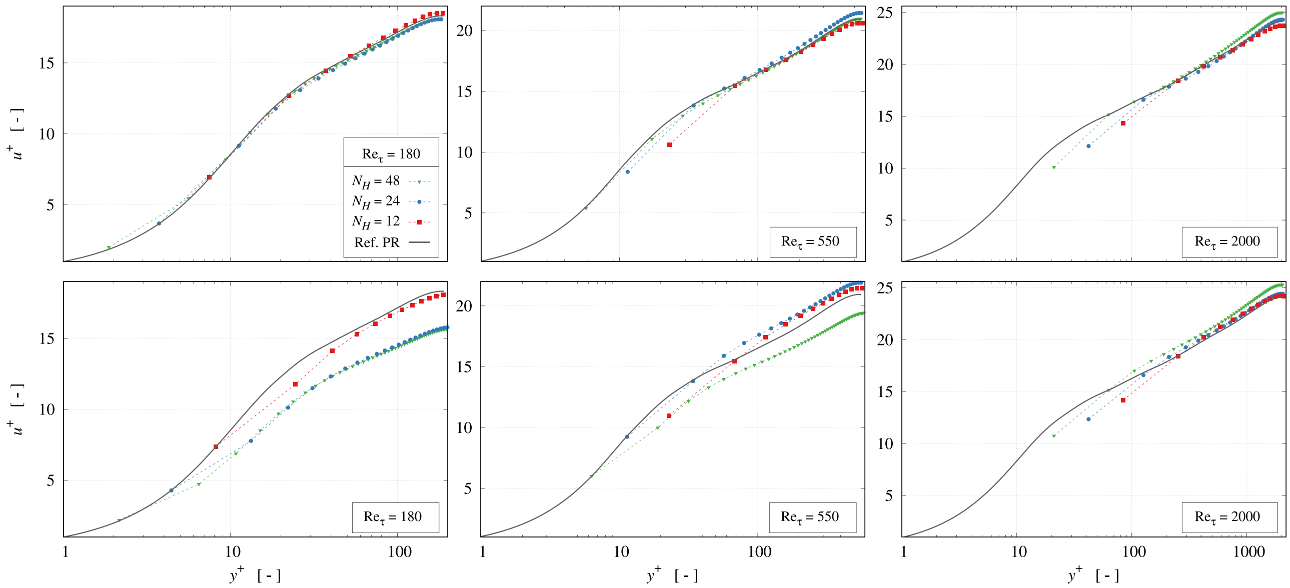

FIG. 32. Predicted mean velocity profiles for $\mathrm{Re}_\tau = \{180; 550; 2000\}$ in comparison with reference data[60,61] (Ref. PR) for the present (top) SGS and a fixed Smagorinsky constant (bottom, $\mathscr{C}_S = 0.15$) approach.

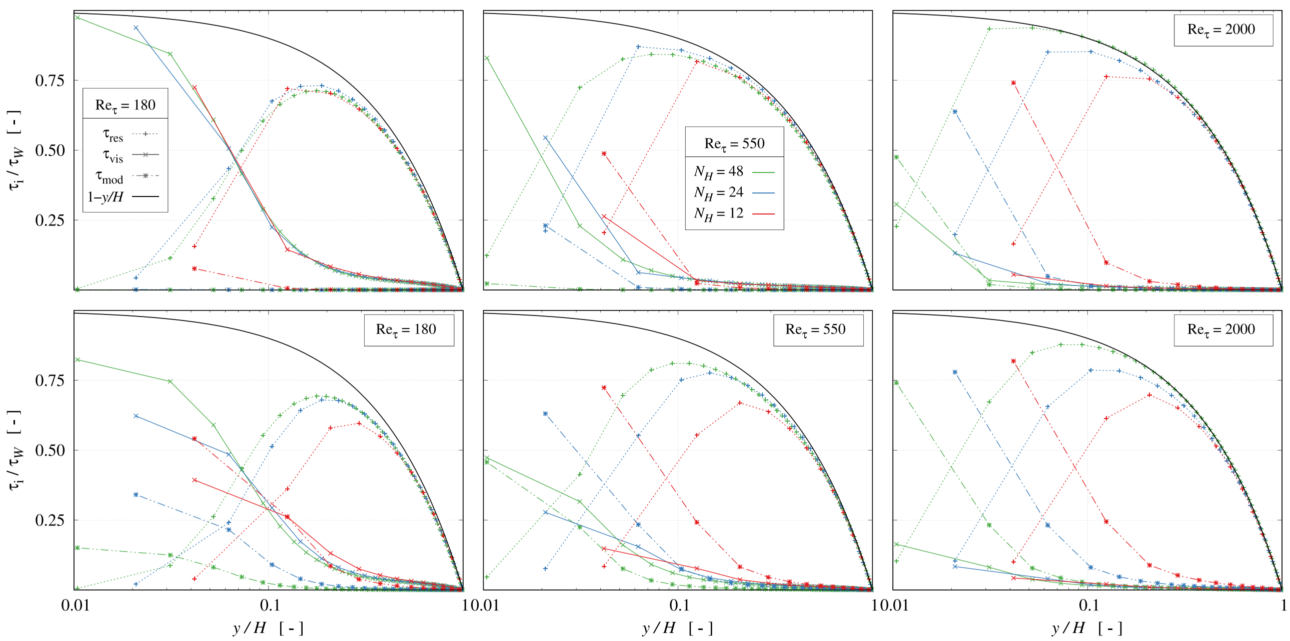

FIG. 33. Comparison of non-dimensional resolved (dotted), viscous (solid), and modeled (dashed) shear stress profiles with a linear total stress relation $\tau_i/\tau_W = 1 - y/H$ (solid black line) for the present (top) SGS and a fixed Smagorinsky constant (bottom, $\mathscr{C}_S = 0.15$) approach.

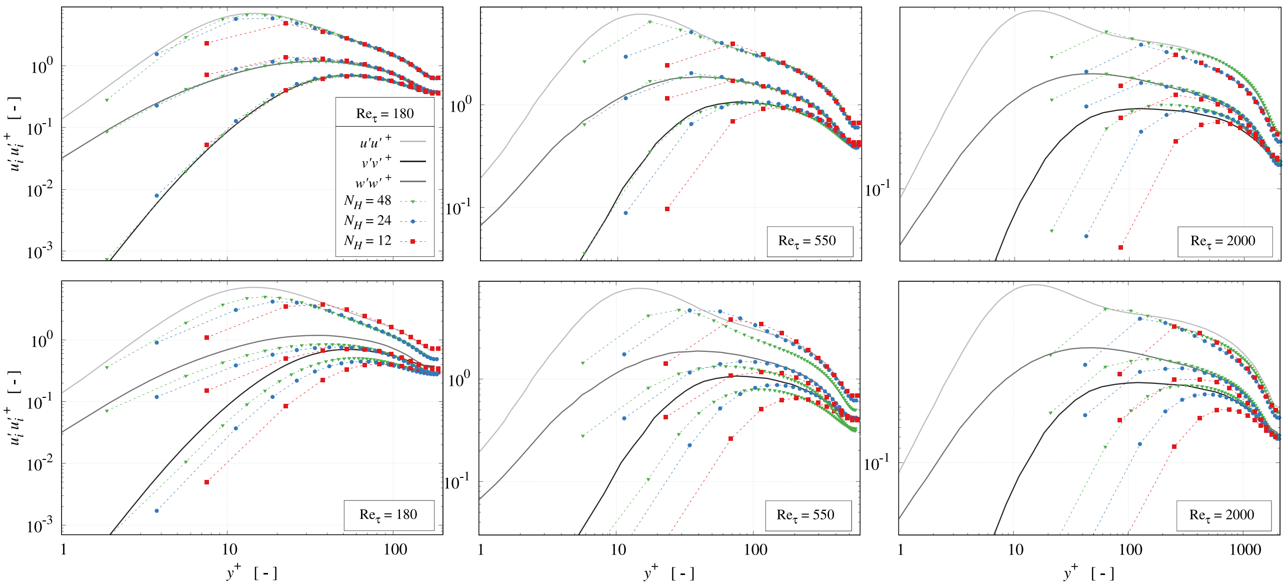

FIG. 34. Resolved Reynolds normal stresses predicted by the present (top) SGS and a fixed Smagorinsky constant (bottom, $\mathscr{C}_S = 0.15$) approach, supplemented by reference data.[60,61]

$$a_4 = (1/\omega_1 - 1/2)\, A\, \rho. \tag{B25}$$

Likewise, fourth-order related relaxations are defined via

$$C^*_{211} = (1 - \omega_1/2)\, B\, C_{011}, \tag{B26}$$

$$C^*_{121} = (1 - \omega_1/2)\, B\, C_{101}, \tag{B27}$$

$$C^*_{112} = (1 - \omega_1/2)\, B\, C_{110}. \tag{B28}$$

The capitalized parameters are as follows:

$$A = \frac{-3\omega_1^2 + 2\omega_1 + 4}{5\omega_1^2 - 7\omega_1 + 2} \quad \text{and} \quad B = \frac{-14\omega_1^2 + 28\omega_1 + 4}{15\omega_1^2 - 21\omega_1 + 6}. \tag{B29}$$

It is noted that these two expressions (B29) are simplified and only valid on the condition of $\omega_2 = 1$ since the primal equations hold for $A[B] = A[B](\omega_1, \omega_2)$. The fifth- and sixth-order cumulants are set to zero, implying their nonequilibria are completely erased during collision,

$$C^*_{221} = 0, \; C^*_{212} = 0, \; C^*_{122} = 0, \; C^*_{222} = 0. \tag{B30}$$

Optional body forces $\boldsymbol{F}$ are incorporated by shifting the frame of reference in terms of $\boldsymbol{u} = \boldsymbol{u} + \Delta t\, \boldsymbol{F}/(2\rho)$.

APPENDIX C: COMPARISON OF PRESENT DYNAMIC AND A CONVENTIONAL SMAGORINSKY APPROACH

Figures 32–34 compare the results obtained from the present cumulant based (top) and a conventional (bottom, using $\mathscr{C}_S = 0.15$ following Pope[86]) Smagorinsky approach for $\mathrm{Re}_\tau = \{180; 550; 2000\}$ and $\mathrm{Ma} = 0.1$.

REFERENCES

[1] R. Kotapati, A. Keatin, S. Kandasamy, B. Duncan, R. Shock, and H. Chen, "The lattice-Boltzmann-VLES method for automotive fluid dynamics simulation, a review," Technical Report No. 2009-26-0057 (SAE, 2009).

[2] S. Noelting and E. Fares, "The lattice-Boltzmann method: An alternative to LES for complex aerodynamic and aeroacoustic simulations in the aerospace industry," Technical Report No. 2015-01-2575 (SAE, 2015).

[3] C. Niedermeier, C. Janßen, and T. Indinger, "Massively-parallel multi-GPU simulations for fast and accurate automotive aerodynamics," in Proceedings of the 7th European Conference on Computational Fluid Dynamics, Glasgow, 11–15 June (2018).

[4] S. Lenz, M. Schönherr, M. Geier, M. Krafczyk, A. Pasquali, A. Christen, and M. Giometto, "Towards real-time simulation of turbulent air flow over a resolved urban canopy using the cumulant lattice Boltzmann method on a GPGPU," J. Wind Eng. Ind. Aerodyn. **189**, 151–162 (2019).

[5] J. Boudet, E. Lévôque, and H. Touil, "Unsteady lattice Boltzmann simulations of corner separation in a compressor cascade," J. Turbomach. **144**, 011010 (2021).

[6] M. Geier, A. Greiner, and J. Korvink, "Cascaded digital lattice Boltzmann automata for high Reynolds number flow," Phys. Rev. E **73**, 066705 (2006).

[7] W. Abdel Kareem, S. Izawa, A. Xiong, and Y. Fukunishi, "Lattice Boltzmann simulations of homogeneous isotropic turbulence," Comput. Math. Appl. **58**, 1055–1061 (2009).

[8] C. Aidun and J. Clausen, "Lattice-Boltzmann method for complex flows," Annu. Rev. Fluid Mech. **42**, 439–472 (2010).

[9] S. Chikatamarla, C. Frouzakis, I. Karlin, A. Tomboulides, and K. Boulouchos, "Lattice Boltzmann method for direct numerical simulation of turbulent flows," J. Fluid Mech. **656**, 298–308 (2010).

[10] L. Jahanshaloo, E. Pouryazdanpanah, and N. C. Sidik, "A review on the application of the lattice Boltzmann method for turbulent flow simulation," Numer. Heat Transfer, Part A **64**, 938–953 (2013).

[11] K. Suga, Y. Kuwata, K. Takashima, and R. Chikasue, "A D3Q27 multiple-relaxation-time lattice Boltzmann method for turbulent flows," Comput. Math. Appl. **69**, 518–529 (2015).

[12] M. Geier, A. Pasquali, and M. Schönherr, "Parametrization of the cumulant lattice Boltzmann method for fourth order accurate diffusion. II. Application to flow around a sphere at drag crisis," J. Comput. Phys. **348**, 889–898 (2017).

[13] A. Banari, M. Gehrke, C. Janßen, and T. Rung, "Numerical simulation of nonlinear interactions in a naturally transitional flat plate boundary layer," Comput. Fluids **203**, 104502 (2020).

[14] M. Gehrke, C. Janßen, and T. Rung, "Scrutinizing lattice Boltzmann methods for direct numerical simulations of turbulent channel flows," Comput. Fluids **156**, 247–263 (2017).

[15]P. Nathen, D. Gaudlitz, M. Krause, and N. Adams, "On the stability and accuracy of the BGK, MRT and RLB Boltzmann schemes for the simulation of turbulent flows," Commun. Comput. Phys. **23**, 846–876 (2018).
[16]M. Geier, S. Lenz, M. Schönherr, and M. Krafczyk, "Under-resolved and large eddy simulations of a decaying Taylor-Green vortex with the cumulant lattice Boltzmann method," Theor. Comput. Fluid Dyn. **35**, 169–208 (2021).
[17]I. Ginzburg, F. Verhaeghe, and D. d'Humières, "Two-relaxation-time lattice Boltzmann scheme: About parametrization, velocity, pressure and mixed boundary conditions," Commun. Comput. Phys. **3**, 427–478 (2008).
[18]F. Bösch, S. Chikatamarla, and I. Karlin, "Entropic multirelaxation lattice Boltzmann models for turbulent flows," Phys. Rev. E **92**, 043309 (2015).
[19]P. Bhatnagar, E. Gross, and M. Krook, "A model for collision processes in gases. I. Small amplitude processes in charged and neutral one-component systems," Phys. Rev. **94**, 511–525 (1954).
[20]D. d'Humières, I. Ginzburg, M. Krafczyk, P. Lallemand, and L. Luo, "Multiple-relaxation-time lattice Boltzmann models in three dimensions," Philos. Trans. R. Soc. A **360**, 437–451 (2002).
[21]S. Seeger and K. Hoffmann, "The cumulant method for computational kinetic theory," Continuum Mech. Thermodyn. **12**, 403–421 (2000).
[22]M. Geier, M. Schönherr, A. Pasquali, and M. Krafczyk, "The cumulant lattice Boltzmann equation in three dimensions: Theory and validation," Comput. Math. Appl. **70**, 507–547 (2015).
[23]C. Coreixas, G. Wissocq, B. Chopard, and J. Latt, "Impact of collision models on the physical properties and the stability of lattice Boltzmann methods," Philos. Trans. R. Soc. A **378**, 20190397 (2020).
[24]A. Pasquali, M. Geier, and M. Krafczyk, "Near-wall treatment for the simulation of turbulent flow by the cumulant lattice Boltzmann method," Comput. Math. Appl. **79**, 195–212 (2020).
[25]M. Gehrke, A. Banari, and T. Rung, "Performance of under-resolved, model-free LBM simulations in turbulent shear flows," in *Progress in Hybrid RANS-LES Modelling*, edited by Y. Hoarau, S. Peng, D. Schwamborn, A. Revell, and C. Mockett (Springer International Publishing, Cham, 2020), pp. 3–18.
[26]M. Gehrke and T. Rung, "Periodic hill flow simulations with a parameterized cumulant lattice Boltzmann method," Int. J. Numer. Methods Fluids **94**(8), 1111–1154 (2022).
[27]M. Geier, A. Pasquali, and M. Schönherr, "Parametrization of the cumulant lattice Boltzmann method for fourth order accurate diffusion. I. Derivation and validation," J. Comput. Phys. **348**, 862–888 (2017).
[28]X. He and L. Luo, "Theory of the lattice Boltzmann method: From the Boltzmann equation to the lattice Boltzmann equation," Phys. Rev. E **56**, 6811–6817 (1997).
[29]S. Chen and G. Doolen, "Lattice Boltzmann method for fluid flows," Annu. Rev. Fluid Mech. **30**, 329–364 (1998).
[30]S. Succi, *The Lattice Boltzmann Equation: For Fluid Dynamics and Beyond* (Oxford University Press, 2001).
[31]A. A. Mohamad, *Lattice Boltzmann Method* (Springer, 2011).
[32]T. Krüger, H. Kusumaatmaja, A. Kuzmin, O. Shardt, A. Silva, and E. Viggen, *The Lattice Boltzmann Method* (Springer International Publishing, Switzerland, 2017).
[33]C. Janßen, D. Mierke, M. Überrück, S. Gralher, and T. Rung, "Validation of the GPU-accelerated CFD solver ELBE for free surface flow problems in civil and environmental engineering," Computation **3**, 354–385 (2015).
[34]Y. Qian, D. d'Humières, and P. Lallemand, "Lattice BGK models for Navier Stokes equation," Europhys. Lett. **17**, 479–784 (1992).
[35]D. Yu, R. Mei, L. Luo, and W. Shyy, "Viscous flow computations with the method of lattice Boltzmann equation," Prog. Aerosp. Sci. **39**, 329–367 (2003).
[36]J. Smagorinsky, "General circulation experiments with the primitive equations," Mon. Weather Rev. **91**, 99–164 (1963).
[37]M. Germano, U. Piomelli, P. Moin, and W. Cabot, "A dynamic subgrid-scale eddy viscosity model," Phys. Fluids A **3**, 1760–1765 (1991).
[38]S. Girimaji, "Boltzmann kinetic equation for filtered fluid turbulence," Phys. Rev. Lett. **99**, 034501 (2007).
[39]P. Sagaut, "Toward advanced subgrid models for lattice-Boltzmann-based large-eddy simulation: Theoretical formulations," Comput. Math. Appl. **59**, 2194–2199 (2010).
[40]H. Asmuth, H. Olivares-Espinosa, and S. Ivanell, "Actuator line simulations of wind turbine wakes using the lattice Boltzmann method," Wind Energy Sci. **5**, 623–645 (2020).
[41]H. Asmuth, C. Janßen, H. Olivares-Espinosa, and S. Ivanell, "Wall-modeled lattice Boltzmann large-eddy simulation of neutral atmospheric boundary layers," Phys. Fluids **33**, 105111 (2021).
[42]S. Hou, J. Sterling, S. Chen, and G. Doolen, "A lattice Boltzmann subgrid model for high Reynolds number flows," in *Pattern Formation and Lattice Gas Automata*, edited by A. Lawniczak and R. Kapral (American Mathematical Society, 1995), pp. 1–18.
[43]M. Krafczyk, J. Tölke, and L. Luo, "Large-eddy simulations with a multiple-relaxation-time LBE model," Int. J. Mod. Phys. B **17**, 33–39 (2003).
[44]H. Yu, L. Luo, and S. Girimaji, "LES of turbulent square jet flow using an MRT lattice Boltzmann model," Comput. Fluids **35**, 957–965 (2006).
[45]N. Onodera and T. Aoki, "Large-eddy simulation of turbulent flow around a car body using lattice Boltzmann method on the TSUBAME supercomputer," in Proceedings of the 11th World Congress on Computational Mechanics (WCCM), Barcelona, 20–25 July (2014).
[46]M. Han, R. Ooka, and H. Kikumoto, "Lattice Boltzmann method-based large-eddy simulation of indoor isothermal airflow," Int. J. Heat Mass Transfer **130**, 700–709 (2019).
[47]M. Haussmann, F. Ries, J. Jeppener-Haltenhoff, Y. Li, M. Schmidt, C. Welch, L. Illmann, B. Böhm, H. Nirschl, M. Krause, and A. Sadiki, "Evaluation of a near-wall-modeled large eddy lattice Boltzmann method for the analysis of complex flows relevant to IC engines," Computation **8**, 43 (2020).
[48]Y. Feng, J. Miranda-Fuentes, S. Guo, J. Jacob, and P. Sagaut, "ProLB: A lattice Boltzmann solver of large-eddy simulation for atmospheric boundary layer flows," J. Adv. Model. Earth Syst. **13**, e2020MS002107 (2021).
[49]C. Teixeira, "Incorporating turbulence models into the lattice-Boltzmann method," Int. J. Mod. Phys. C **09**, 1159–1175 (1998).
[50]M. Haussmann, A. Claro Barreto, G. Lipeme Kouyi, N. Rivière, H. Nirschl, and M. Krause, "Large-eddy simulation coupled with wall models for turbulent channel flows at high Reynolds numbers with a lattice Boltzmann method—Application to Coriolis mass flowmeter," Comput. Math. Appl. **78**, 3285–3302 (2019).
[51]M. Gaedtke, S. Wachter, M. Rädle, H. Nirschl, and M. Krause, "Application of a lattice Boltzmann method combined with a Smagorinsky turbulence model to spatially resolved heat flux inside a refrigerated vehicle," Comput. Math. Appl. **76**, 2315–2329 (2018).
[52]M. Han, R. Ooka, and H. Kikumoto, "A wall function approach in lattice Boltzmann method: Algorithm and validation using turbulent channel flow," Fluid Dyn. Res. **53**, 045506 (2021).
[53]M. Breuer, N. Peller, C. Rapp, and M. Manhart, "Flow over periodic hills—Numerical and experimental study in a wide range of Reynolds numbers," Comput. Fluids **38**, 433–457 (2009).
[54]S. Ghosal, T. Lund, P. Moin, and K. Akselvoll, "A dynamic localization model for large-eddy simulation of turbulent flows," J. Fluid Mech. **286**, 229–255 (1995).
[55]M. Han, R. Ooka, and H. Kikumoto, "Effects of wall function model in lattice Boltzmann method-based large-eddy simulation on built environment flows," Build. Environ. **195**, 107764 (2021).
[56]J. Degrigny, S. Cai, J. Boussuge, and P. Sagaut, "Improved wall model treatment for aerodynamic flows in LBM," Comput. Fluids **227**, 105041 (2021).
[57]H. Maeyama, T. Imamura, J. Osaka, and N. Kurimoto, "Unsteady turbulent flow simulation using lattice Boltzmann method with near-wall modeling," AIAA Paper No. 2020-2565, 2020.
[58]H. Maeyama, T. Imamura, J. Osaka, and N. Kurimoto, "Turbulent channel flow simulations using the lattice Boltzmann method with near-wall modeling on a non-body-fitted Cartesian grid," Comput. Math. Appl. **93**, 20–31 (2021).
[59]H. Maeyama, T. Imamura, J. Osaka, and N. Kurimoto, "Application of wall-modeled large-eddy simulation based on lattice Boltzmann method to external flow analyses," AIAA Paper No. 2021-0458, 2021.
[60]R. Moser, J. Kim, and N. Mansour, "Direct numerical simulation of turbulent channel flow up to $Re_\tau \approx 590$," Phys. Fluids **11**, 943–945 (1999).
[61]M. Bernardini, S. Pirozzoli, and P. Orlandi, "Velocity statistics in turbulent channel flow up to $Re_\tau = 4000$," J. Fluid Mech. **742**, 171–191 (2014).
[62]D. Spalding, "A single formula for the law of wall," J. Appl. Mech. **28**, 455–458 (1961).
[63]T. Rung, H. Lübcke, and F. Thiele, "Universal wall-boundary conditions for turbulence-transport models," Z. Angew. Math. Mech. **81**, 481–482 (2001).
[64]A. Musker, "Explicit expression for the smooth wall velocity distribution in a turbulent boundary layer," AIAA J. **17**, 655–657 (1979).

[65]H. Werner and H. Wengle, "Large-eddy simulation of turbulent flow over and around a cube in a plate channel," in *Turbulent Shear Flows 8*, edited by F. Durst, R. Friedrich, B. Launder, F. Schmidt, U. Schumann, and J. Whitelaw (Springer, Berlin, Heidelberg, 1993), pp. 155–168.
[66]T. Shih, L. Povinelli, N. Liu, M. Potapczuk, and J. Lumley, "A generalized wall function," Technical Report No. NASA/TM-1999-209398, 1999.
[67]T. Shih, L. Povinelli, and N. Liu, "Application of generalized wall function for complex turbulent flows," in *Engineering Turbulence Modelling and Experiments 5*, edited by W. Rodi and N. Fueyo (Elsevier Science Ltd., Oxford, 2002), pp. 177–186.
[68]U. Schumann, "Subgrid scale model for finite difference simulations of turbulent flows in plane channels and annuli," J. Comput. Phys. **18**, 376–404 (1975).
[69]X. Yang, G. Park, and P. Moin, "Log-layer mismatch and modeling of the fluctuating wall stress in wall-modeled large-eddy simulations," Phys. Rev. Fluids **2**, 104601 (2017).
[70]C. Moeng, "A large-eddy-simulation model for the study of planetary boundary-layer turbulence," J. Atmos. Sci. **41**, 2052–2062 (1984).
[71]J. Albertson and M. Parlange, "Surface length scales and shear stress: Implications for land-atmosphere interaction over complex terrain," Water Resour. Res. **35**, 2121–2132, https://doi.org/10.1029/1999WR900094 (1999).
[72]B. Maronga, C. Knigge, and S. Raasch, "An improved surface boundary condition for large-eddy simulations based on Monin–Obukhov similarity theory: Evaluation and consequences for grid convergence in neutral and stable conditions," Boundary Layer Meteorol. **174**, 297–325 (2020).
[73]D. Yu, R. Mei, and W. Shyy, "A unified boundary treatment in lattice Boltzmann method," AIAA Paper No. 2003-0953, 2003.
[74]M. Bouzidi, M. Firdaouss, and P. Lallemand, "Momentum transfer of a Boltzmann-lattice fluid with boundaries," Phys. Fluids **13**, 3452–3459 (2001).
[75]S. Wilhelm, J. Jacob, and P. Sagaut, "An explicit power-law-based wall model for lattice Boltzmann method-Reynolds-averaged numerical simulations of the flow around airfoils," Phys. Fluids **30**, 065111 (2018).
[76]Y. Chen, Q. Cai, Z. Xia, M. Wang, and S. Chen, "Momentum-exchange method in lattice Boltzmann simulations of particle-fluid interactions," Phys. Rev. E **88**, 013303 (2013).
[77]Y. Dubief and F. Delcayre, "On coherent-vortex identification in turbulence," J. Turbul. **11**, N11 (2000).
[78]R. Dean, "Reynolds number dependence of skin friction and other bulk flow variables in two-dimensional rectangular duct flow," J. Fluids Eng. **100**, 215–223 (1978).
[79]S. Banerjee, R. Krahl, F. Durst, and C. Zenger, "Presentation of anisotropy properties of turbulence, invariants versus eigenvalue approaches," J. Turbul. **8**, N32 (2007).
[80]J. Cooley and J. Tukey, "An algorithm for the machine calculation of complex Fourier series," Math. Comput. **19**, 297–301 (1965).
[81]F. Harris, "On the use of windows for harmonic analysis with the discrete Fourier transform," Proc. IEEE **66**, 51–83 (1978).
[82]J. Kim, P. Moin, and R. Moser, "Turbulence statistics in fully developed channel flow at low Reynolds number," J. Fluid Mech. **177**, 133–166 (1987).
[83]M. Lee and R. Moser, "Direct numerical simulation of turbulent channel flow up to $Re_\tau \approx 5200$," J. Fluid Mech. **774**, 395–415 (2015).
[84]J. Brasseur and T. Wei, "Designing large-eddy simulation of the turbulent boundary layer to capture law-of-the-wall scaling," Phys. Fluids **22**, 021303 (2010).
[85]D. Tritton, "Some new correlation measurements in a turbulent boundary layer," J. Fluid Mech. **28**, 439–462 (1967).
[86]S. Pope, *Turbulent Flows* (Cambridge University Press, 2000).